Corrosion behavior of Al-containing MAX-phase coatings exposed to oxygen containing molten Pb at 600 °C

Hao Shi[a,b,*], Raheleh Azmi[c,d], Liuliu Han[e], Chongchong Tang[c,*], Alfons Weisenburger[a], Annette Heinzel[a], Julia Maibach[c], Michael Stüber[c], Kangli Wang[b], Georg Müller[a]

[a] *Institute for Pulsed Power and Microwave Technology (IHM), Karlsruhe Institute of Technology (KIT), Hermann-von-Helmholtz-Platz 1, 76344 Eggenstein-Leopoldshafen, Germany*

[b] *State Key Laboratory of Advanced Electromagnetic Engineering and Technology, School of Electrical and Electronic Engineering, Huazhong University of Science and Technology, Wuhan 430074, PR China*

[c] *Institute for Applied Materials (IAM), Karlsruhe Institute of Technology (KIT), Hermann- von-Helmholtz-Platz 1, 76344 Eggenstein-Leopoldshafen, Germany*

[d] *Department of Chemistry-Ångström Laboratory, Structural Chemistry, Uppsala University (UU), Lägerhyddsvägen 1, 75121 Uppsala, Sweden*

[e] *Max-Planck-Institut für Eisenforschung, Max-Planck-Straße 1, 40237 Düsseldorf, Germany*

* Corresponding author. E-mail address: hao.shi@kit.edu (H. Shi); chongchong.tang@kit.edu (C.C. Tang).

Abstract: Four types of MAX-phase coating samples (Cr_2AlC, V_2AlC, Ti_2AlC, and Ti_3AlC_2), synthesized via physical vapor deposition and post-annealing of elemental multilayer films, have been investigated toward their potential corrosion protection in 10^{-6} wt.% oxygen-containing molten Pb for 3200 h at 600 °C. Three MAX-phase coatings (Cr_2AlC, Ti_2AlC, and Ti_3AlC_2) are corrosion resistant against the molten Pb, via formation of a protective oxide layer. Specifically, various oxide scales formed on each sample: an Al_2O_3 scale, containing a low amount of Cr_2O_3 was formed in case of the Cr_2AlC coating; a mixed Al_2O_3 and TiO_2 oxide scale was observed for both Ti_2AlC and Ti_3AlC_2 coatings. A more complex mixed oxide layer consisting of VO_2, V_4O_7, and $Pb_3(VO_4)_2$ phases is formed on the V_2AlC coating, while the MAX-phase coating was almost entirely consumed. According to their corrosion performance against oxygen containing molten Pb, the order of corrosion resistance is: $Cr_2AlC > Ti_2AlC > Ti_3AlC_2 > V_2AlC$.

Keywords: MAX-phase coating; Corrosion; Heavy liquid metal; Oxide scale.

1. Introduction

The increasing demands on energy and the necessity to reduce environmental pollutions urge humans to look for environmental friendly and more efficient energy production technologies, including advanced Gen IV fast-neutron fission reactors [1-5], accelerator-driven systems (ADS) [6], concentrated solar power (CSP) plant [1-3], liquid metal batteries (LMB) [7]. On the other side, these advanced systems often employ heavy liquid metals (HLMs), namely Pb or Pb-Bi eutectic (LBE), as the thermal transfer or storage media because of their promising thermo-physical, thermo-hydraulic and neutronic properties [8-10]. However, the compatibility of structural steels (e.g.

ferritic/martensitic and austenitic steels) with HLMs, especially the corrosion properties, challenges the application of HLMs. Moreover, the corrosion attack is accelerated when the operating temperature is above 500 °C [11-16]. Therefore, it is necessary to develop advanced corrosion resistant materials or coatings, like alumina-forming austenitic steels and MAX-phase materials/coatings [15-19].

One type of layered ternary compounds, also known as MAX-phase materials [17], with the formula $M_{n+1}AX_n$ (n=1 to 3), where M belongs to an early transition metal, A is an A-group (mostly IIIA and IVA) element, and X can be C or N, shows the excellent oxidation/corrosion resistance at elevated temperature, good thermo-physical and thermal stability properties [18-23]. Their crystal structures can be described as different MX layers interleaved with pure-A element layers. The specific nanolayered structure and bonding characteristics endow them to possess both metallic and ceramic properties [17-21].

In general, the oxidation resistance is related with the formation of a dense and continuous oxide layer acting as an elemental diffusion barrier, such as Al_2O_3, Cr_2O_3, or/and potentially mixed oxide scale [15, 16, 18-21]. Of particular interest of current work are alumina-forming or aluminum-containing MAX-phases (e.g. Cr_2AlC, Ti_2AlC, V_2AlC, Ti_3AlC_2) when considering the high thermal stability of an Al_2O_3 rich oxide scale [15-16, 18-21].

The high-temperature oxidation of aluminum-containing MAX-phases has been extensively investigated [19, 21, 24-29]. However, the reported corrosion/oxidation tests are mainly performed in air or water containing environments. Lee et al. [24] studied the oxidation behavior of Cr_2AlC in the temperature range of 700 to 1000 °C in air. An Al_2O_3 layer together with a sub-layer of Cr_7C_3 has been observed after oxidation tests. The formation of Cr_7C_3 underneath the Al_2O_3 layer is due to the selective oxidation of Al and the strong bond of Cr-C [24-25]. When the oxidation is performed at a lower temperature, a layer of Cr_2O_3 instead of Al_2O_3 is formed, e.g. the oxidation test of Cr_2AlC in simulated primary water at 300 °C [22]. The V_2AlC MAX-phase is also considered due to the low deposition temperature and good irradiation tolerance [26]. In the case of the oxidation in air, a multi-layer structure, consisting of V_2O_5, $AlVO_4$, or/and Al_2O_3, is frequently observed in the temperature range of 600 to 800 °C [26-29]. The morphologies of the oxide layer also vary from needle-like to strip-type grains, depending on the types of oxides formed [26, 29]. The oxide scales formed on Ti_2AlC and Ti_3AlC_2 are mainly dependent on the oxidation temperatures. At exposure temperature above 900 °C, nearly pure alumina scale forms with some TiO_2 particles decorated on the surface [30-35]. However, at low oxidation temperatures, abnormal oxidation behavior has been reported due to the fast growth of TiO_2 with different crystalline structures (anatase and rutile) of TiO_2 [31]. Both inward diffusion of oxygen and outward diffusion of Al and Ti contributes to the

oxidation process [31, 34].

The corrosion tests of Al-containing MAX-phases in HLMs are mainly focused on bulk Ti_2AlC and Ti_3AlC_2 [23, 35-37]. Barnes et al. [35] tested the corrosion behavior of Ti_2AlC samples in oxygen-free molten Pb at 650 and 800 °C, respectively. Their results show that no obvious reaction/interaction happens between the MAX-phase and liquid Pb. Lapauw et al. [36] have investigated the corrosion behavior of Ti_2AlC and Ti_3AlC_2 in oxygen-poor ($C_O < 10^{-8}$ wt.%) and static LBE at 500 °C. A non-uniform and thin oxide scale (< 0.5 μm) is observed after 3500 h corrosion exposure. Besides, local corrosion attack in terms of LBE penetration has been observed after 3500 h exposure, mainly caused by the preferential dissolving of parasitic phases like $TiAl_3$ [36]. A similar result was obtained by Heinzel et al. [37]. Above 550 °C with an oxygen content of 10^{-8} wt.% in the molten LBE, the Ti_2AlC shows LBE penetration between the large plate-like Ti_2AlC grains due to the corrosion of secondary phases, the Ti_2AlC grains themselves seem to be corrosion resistant. Besides, Heinzel et al. [37] also tested the corrosion behavior of Ti_2AlC in 10^{-6} wt.% oxygen-containing molten LBE at 550, 650, and 700 °C. At 550 °C a mixed oxide layer consisting of TiO_2 (rutile), Pb, Bi, and Al is formed after 10000 h. At higher temperatures, an Al_2O_3 outer layer followed by a TiO_2 inner layer protects the material.

Previous results indicate that MAX-phase coatings with single phase can be prepared by magnetron sputtering plus post annealing of nanoscale multilayers [20-21, 26, 38]. No reports on the corrosion behavior of MAX-phase coatings in HLMs are avilable up to now. Considering the promising corrosion/oxidation behavior of Al-containing MAX-phases like Cr_2AlC, V_2AlC, Ti_2AlC, and Ti_3AlC_2, the motivation of the current work is to investigate the corrosion behavior of such coatings in 10^{-6} wt.% oxygen-containing molten Pb at 600 °C. Moreover, the microstructure of a passivating oxide layer on the sample surface is carefully characterized. The results obtained from different characterization methods (e.g. XRD, GIXRD, XPS, SEM/EDX, TEM) indicate the protectivity and excellent application prospects of MAX-phase coatings, especially the Cr_2AlC and Ti_2AlC, in heavy liquid metal environments.

2. Material and experiment

2.1 MAX-phase coating preparation

Four different types of Al-containing MAX phase coatings were synthesized on polished polycrystalline Al_2O_3 substrates following a two-step process. In the first step, three elemental targets (i.e., transition metal Ti, Cr or V, graphite, and aluminum) were adopted to deposit M/C/Al elemental multilayers with nanostructured designs by magnetron sputtering (Leybold Z 550 coater). The thicknesses of each individual elemental layer are initially calculated based on the stoichiometric ratio (2:1:1 or 3:1:2) of specific MAX phases and theoretical densities of the elements. During deposition, the sample holder was operated in a stop-and-go mode, i.e. it was cycled and held at

each individual target location for different times to achieve the multilayered design. The holding times were defined based on the deposition rates of each material and thickness required for each element layer. The power for the three targets were set at ~200 W, using radio frequency (RF) power supply for the aluminum and transition metal targets, and direct current (DC) power supply for the graphite target. The working pressure of the argon gas was 0.5 Pa. The substrates were not deliberately heated and grounded without applied bias, resulting in a thin film deposition at room temperature. The final coating thicknesses were targeted at ~3 μm by repeating the multilayered stacks. In the second step, the as-deposited multilayered coatings were annealed in a flowing Ar at atmospheric pressure to promote the crystallization of MAX phases via solid-state diffusion reactions using a NETZSCH STA-449 F3 Jupiter thermal balance. The annealing temperatures and duration time are 550 °C / 10 min for Cr_2AlC, 600 °C / 10 min for V_2AlC, 800 °C / 10 min for Ti_2AlC, and 1000 °C / 30 min for Ti_3AlC_2. The heating and cooling rates during the annealing process are fixed at 10 K/min. The detailed information on the deposition and phase/microstructure formation after annealing of the different multilayered coatings has been reported in [38-39].

2.2 Corrosion experiment

The corrosion experiment is performed in COSTA facility, a stagnant molten Pb/PbBi corrosion test equipment [15]. Each sample with a size of 10*10*1 mm is fixed by a Mo-wire and immersed in an alumina crucible containing the molten Pb. The amount of Pb filled in the crucible is 200 g. Based on the oxygen saturation data [8], the oxygen content dissolved in the molten Pb is controlled to 10^{-6} wt.% at 600 °C. This defined oxygen concentration value is adjusted and monitored by the oxygen partial pressure during the experiment. The general process for the corrosion experiment has been described in the literature [15-16]. After 3200 h exposure, the glove box with similar oxygen condition is employed to extract the samples. Then, samples were cooled down to room temperature before the next step treatment. Since there are adherent Pb on the sample surface, the samples are generally cleaned by exposing in a liquid solution of hydrogen peroxide, acetic acid and ethanol (1:1:1). Samples of Cr_2AlC, Ti_2AlC and Ti_3AlC_2 were cleaned for 15 min, while V_2AlC samples were cleaned for 1 h due to a large amout of remaining Pb on the surface.

2.3 Material Characterization

Phase compositions (before and after exposure) are characterized by X-Ray Diffraction (XRD, Seifert PAD II), applying monochromatic Cu Kα1 radiation with λ=0.15409 nm in a θ-2θ geometry (Bragg–Brentano). The voltage and current are 40 kV and 30 mA, respectively. Parameters like scan speed and step size are 0.1 °/min and 0.02°, respectively. Grazing incidence X-ray diffraction (GIXRD) is also employed to characterize the oxide layer with an incident angle of 2° and a scan speed of 0.75 °/min. The Cu Kα1 radiation (λ=0.15409 nm, 45 kV, and 200 mA) is used as a source for diffraction. The surface morphology and cross-sectional structure of the coating/oxide layer has been

characterized by Scanning Electron Microscopy (SEM, model: Zeiss LEO 1530 VP), equipped with EDX (electron dispersive X-ray spectroscopy). The energy of the electron beam is in the range of 10 to 20 keV with a working distance around 9 mm. In case of the sample cross section analysis, a Ni-layer (~25 μm) is electroplated on the sample surface to protect the surface oxide layer during the SEM specimen preparation (e.g. grinding and polishing). Then, samples are embedded/fixed in resin, and ground with sand papers, e.g. surface finish of 1200 #, 2400 #, followed by polishing with diamond paste up to 1 μm particle size. A thin gold-palladium (AuPd) layer is sputtered on the SEM specimen surface to increase the electrical conductivity.

A K-Alpha+ instrument (Thermo Fisher Scientific) with a monochromatic Al-Kα X-ray source (1486.6 eV) is used for XPS measurements. The X-ray spot size was 400 μm. Charge neutralization is performed by K-Alpha+ charge compensation system using 8 eV electrons and low-energy Ar ions. Data acquisition and processing are accomplished with the software of Thermo Advantage. The spectra are deconvoluted with one or more Voigt profiles [40]. The C 1s peak of adventitious hydrocarbons with binding energy of 285.0 eV has been used as a reference. Besides, three parameters namely Scofield sensitivity factors [41], analyzer transmission function as well as the effective attenuation lengths (EALs) have been employed for the quantification. EALs are calculated based on the standard TPP-2 M formalism [42]. For the depth profiling of samples, monoatomic Ar ions mainly with 4 keV energy, and low current are used. If other energies are used, it is specified in the main text.

In order to help better understand the phase, checmical compositions and microsturucture of the oxide layer, TEM analysis was performed on selected exposed samples. The thin lamellae for TEM investigations were prepared in an FEI Helios 600 crossbeam focused ion beam (FIB) at 30 kV down to an ion current of approximately 24 pA. A Pt layer (around 2 μm) was deposited on the sample surface to protect the oxide scale. The lamellae was cut perpendicularly to the sample surface with a depth around 6 μm. After "lift out" process, the specimen was milled until the oxide layer region becomes transparent. Transmission electron microscopy (TEM) analysis was performed in a Jeol JEM 2100Plus electron microscope with 200 kV acceleration voltage. The bright-field (BF) images and selected area electron diffraction (SAED) characterization were performed in conventional TEM mode. EDS maps were acquired in the scanning transmission electron micrographs (STEM) mode (ca. 60 min acquisition time for each map).

3. Results

3.1 Pristine samples

Figure 1 displays XRD results of all MAX phase samples before the corrosion test. Except for the diffraction signal from the alumina substrate, all other diffraction peaks can be indexed to the

corresponding characteristic MAX phases. The absence of diffraction signals from common impurity phases (for instance binary intermetallics and carbides) confirms the formation of pure MAX phase coatings after thermal annealing for all of these four different systems. In addition, XRD patterns only show the diffraction signals characteristic of (001) lattice planes of a specific MAX phase, which indicates their highly basal-plane textured structure. The diffraction peaks associated with V_2AlC (001) and Cr_2AlC (001) display broad features of lower intensities (compared with the Ti-based MAX phases); their low annealing temperatures adopted (600 °C and 550 °C, respectively) resulted in nanocrystalline structures. In comparison, the relatively high annealing temperatures required for the formation of the Ti_2AlC and Ti_3AlC_2 MAX phases promote the grain growth and their diffraction peaks are more sharp and narrow.
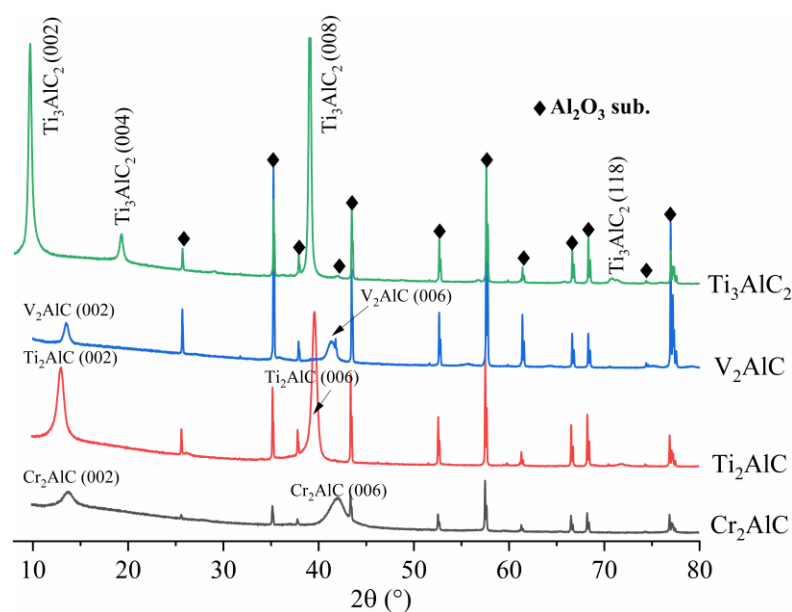

Fig. 1 XRD spectra of prepared MAX-phase coatings in this study before the corrosion test. Reflections marked by a black-filled rhomb are attributed to the alumina substrate.

As an example, the surface morphology of a Ti_2AlC coating is presented in Fig. 2 (a) and (b). A uniform, dense coating is obtained, without an evidence of contaminations, pores, inclusions or other growth defects or coating spallation. A closer look at higher magnification (see Fig. 2 (b), which is an enlarged image of the area marked by a white square in Fig. 2 (a)), confirms these statement. It shows a uniform, homogeneous morphology consisting of nano-sized grains. Fig. 2 (c, d, e, f) show cross-section images of Ti_2AlC, Cr_2AlC, V_2AlC and Ti_3AlC_2 coatings. Fig.2 (c, d) are SEM images and Fig. 2 (e, f) are bright field TEM images showing the grain structure of the MAX phase coatings.

All these coatings display dense, columnar-free structure related to the unique two-step preparation method. The TEM images in Fig.2 (e, f) clearly shows that the coatings consist of platelet-shaped, elongated nanocrystallites, in full coherency with our previously findings [38, 39]. It is necessary to point out that each type of coating has similar grain morphology, but their grain sizes

are different attributed to different annealing temperatures. For instance, the grain size of V_2AlC (~65 nm in length) is much smaller than that of Ti_3AlC_2 (~200 nm in length) due to higher annealing temperature adopted for the Ti_3AlC_2 coatings.
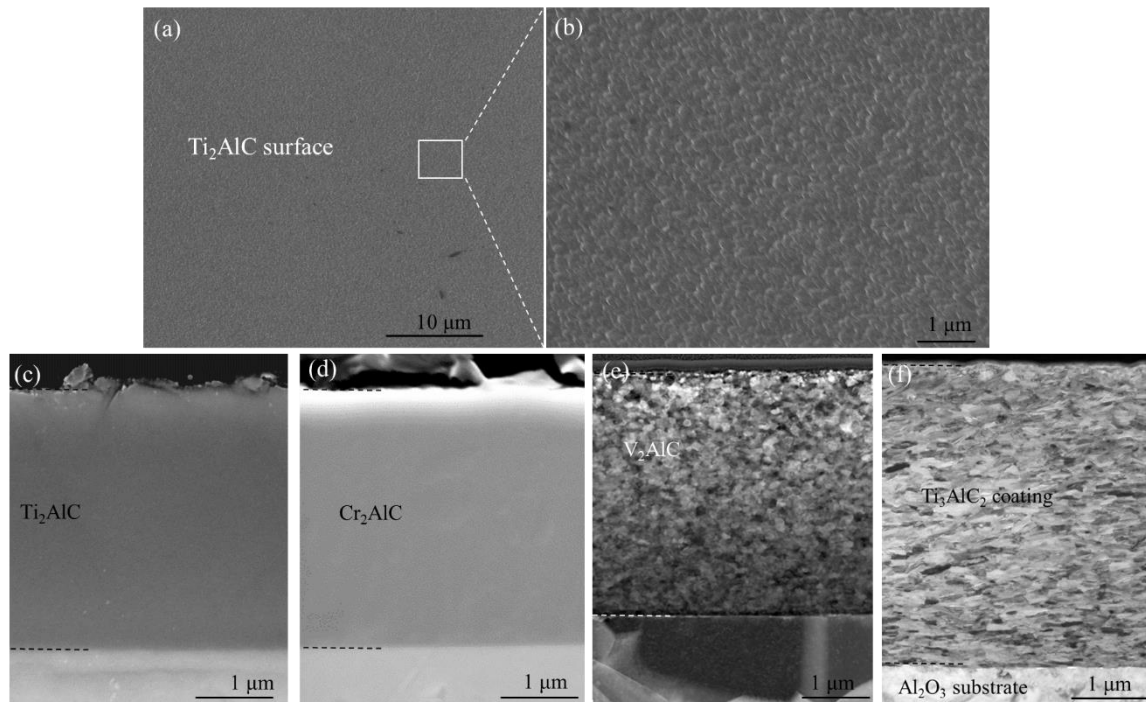

Fig. 2 Surface morphologies of Ti_2AlC coating (a) and englarged image (b); SEM cross sectional images of Ti_2AlC and Cr_2AlC (c, d); bright field TEM cross sectional images of V_2AlC and Ti_3AlC_2 (e, f).

3.2 Materials behavior in molten Pb corrosion test

3.2.1 XRD characterization

Figure 3 displays the results of XRD phase composition analyses of MAX-phase samples exposed to molten Pb at 600°C for 3200 h. In comparison to pristine specimens, additional oxide and carbide phases (like Cr_7C_3, and TiC) have been observed for the exposed samples. While only some samples show carbide formation, all samples exhibit clearly oxide scale formation. Table 1 lists the MAX-phases and other compounds like carbides identified on each sample after the corrosion exposure. In addition, oxide phases are also included in Table 1. The diffraction pattern of the Cr_2AlC sample is the only one that shows the formation of only the α-Al_2O_3 oxide (in corundum structure). All other samples show formation of further, complex oxide phases. However, the Al_2O_3 signals observed in Figure 3 could be either from the oxide layer or the alumina substrate. It is not possible to separate it only by the XRD results obtained here in Bragg-Brentano mode. Both the rutile and anatase phases of TiO_2 have been identified on Ti_2AlC and Ti_3AlC_2 samples, while the anatase signal from the Ti_3AlC_2 sample is quite weak. In the case of V_2AlC, the vanadium oxides with different valences like VO_2 and V_4O_7 have been identified. Besides, the Pb-rich oxides like PbO and $Pb_3(VO_4)_2$ are also obtained. The $Pb_3(VO_4)_2$ phase can be produced by the solid reaction of PbO and V_2O_5 at the
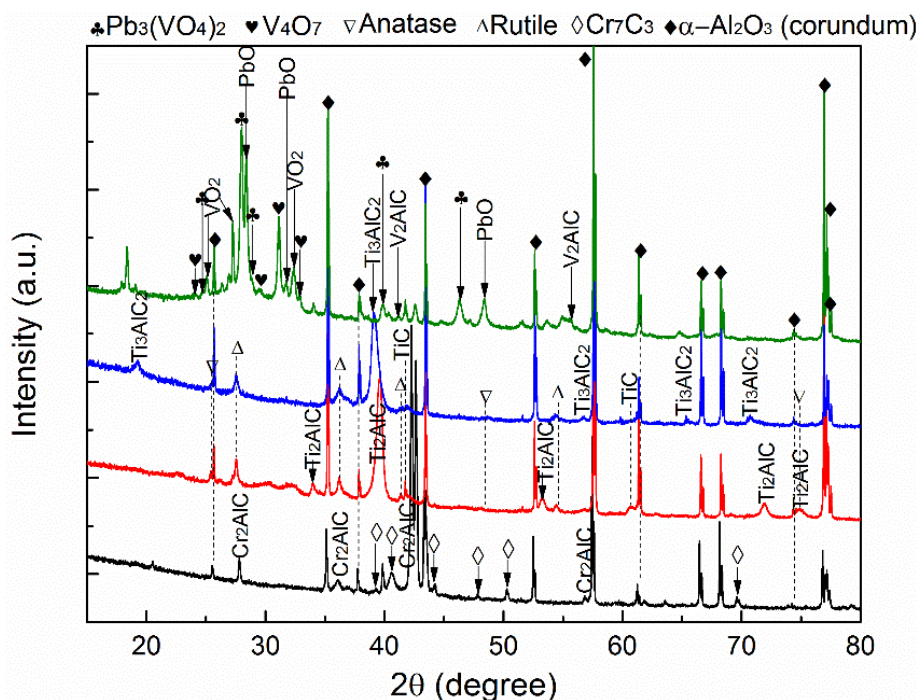
exposure temperature [43].

Fig. 3 XRD spectra of MAX-phase coatings after exposed to molten Pb at 600 °C for 3200 h. Reflections marked by a black-filled rhomb are attributed to the alumina substrate.

Table 1

Phase compositions of MAX-phase coatings after the corrosion test, analyzed with XRD.

Sample code	Phase									
	Cr_2AlC	V_2AlC	Ti_2AlC	Ti_3AlC_2	Cr_7C_3	TiC	α-Al_2O_3	TiO_2	V_xO_y	Other
Cr_2AlC	+	-	-	-	+	-	+	-	-	-
V_2AlC	-	+	-	-	-	-	+	-	+(VO_2, V_4O_7)	$Pb_3(VO_4)_2$, PbO
Ti_2AlC	-	-	+	-	-	+	+	+(Rutile, Anatase)	-	-
Ti_3AlC_2	-	-	-	+	-	+	+	+(Rutile, Anatase)	-	-

+: yes; -: no

Since the oxide scale formed on each MAX-phase coating surface is very thin (MAX phase coatings were not fully oxidized and please also see below cross section analysis), the diffraction patterns obtained from the oxide scale by XRD analyses in the Bragg- Brentano mode are weak. Therefore, the GIXRD technique is applied to examine the phase constitution of the superficial layer

8

of the coated samples only (penetration depth: 0-1000 nm [44]). Fig. 4 shows GIXRD results of the MAX phase coatings after exposure. Compared with Fig. 3, now the diffraction signals from the alumina substrate are greatly suppressed or eliminated. According to the spectra, the same phase $\alpha\text{-}Al_2O_3$ is identified on all three samples, which is located at the same 2θ positions as that detected by the Bragg-Brentano measurements (Fig. 3). In addition, peaks of Cr_2AlC and Cr_7C_3 are also identified for exposed Cr_2AlC coatings. In comparison, V-rich oxides with different stoichiometry are identified on V_2AlC. The phases obtained from the Ti_3AlC_2 sample are mainly the rutile and the MAX phase. The TiC phase is not identified probably due to its low content or/and non-uniform distribution. The Ti_2AlC coating is not checked due to the unsatisfied sample size. Table 2 summarizes the obtained phases by the GIXRD analyses.
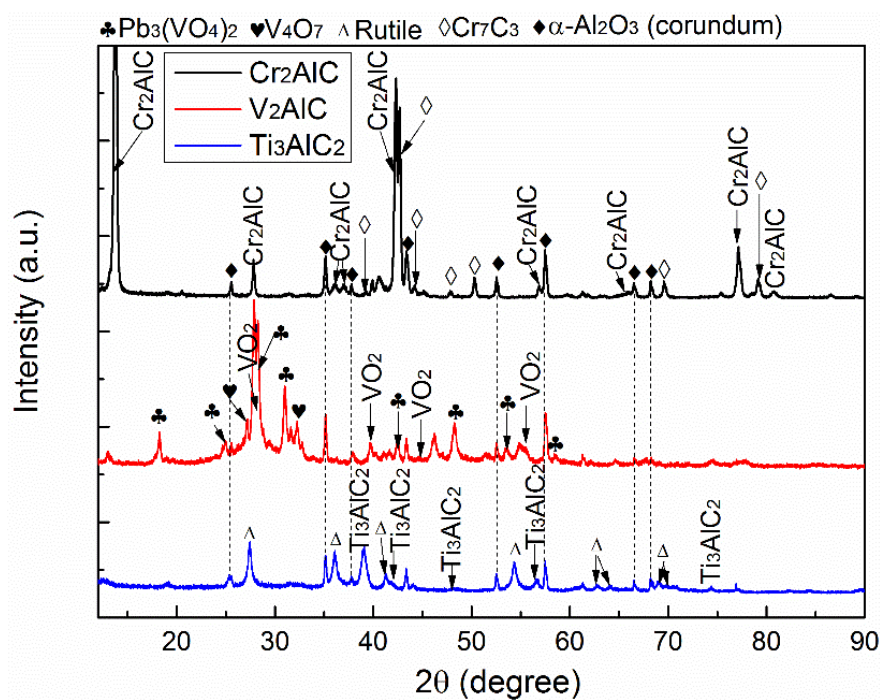
Fig. 4 GIXRD spectra of MAX-phase coatings after the corrosion test. Reflections marked by a black-filled rhomb are attributed to the alumina substrate.

Table 2
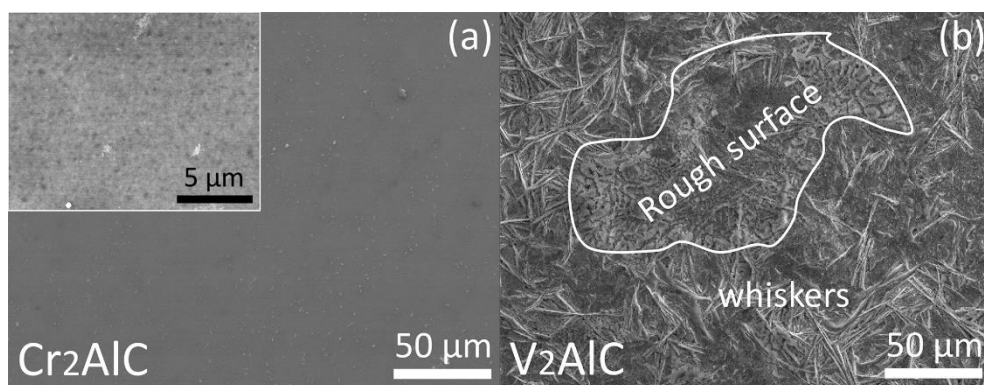Phase compositions of MAX-phase coatings after the corrosion, analyzed by GIXRD.

Sample code	Phase							
	Cr_2AlC	V_2AlC	Ti_3AlC_2	Cr_7C_3	$\alpha\text{-}Al_2O_3$	TiO_2	V_xO_y	Other
Cr_2AlC	+	-	-	+	+	-	-	-
V_2AlC	-	+	-	-	+	-	+(VO_2, V_4O_7)	$Pb_3V_2O_8$,

Ti$_3$AlC$_2$	-	-	+	-	+	+(Rutile)	-	-

+: yes; -: no

3.2.2 Surface analysis

Figure 5 exhibits SEM surface images of samples after the corrosion test. A relatively smooth surface morphology is visible for the Cr$_2$AlC sample. The EDX analysis of the surface composition shows the enriching in O, Al, and Cr, while the Cr concentration is low, see Table 3. For the V$_2$AlC sample, different surface aspects are observed. The general surface shows areas covered by whiskers, which are identified as the remaining Pb even after surface cleaning, as confirmed by the EDX analysis shown in Table 3. Besides, O and V are also detected at the general surface. The concentration of Al is quite lower comparing with the V$_2$AlC MAX phase, shown in Table 3. Among the whisker regions, some areas with a rough surface, either due to the oxide scale exfoliation or the dissolution attack, have been observed. EDX analysis of these parts also reveals high fractions of O, Pb with some V. The surface of Ti$_2$AlC is entirely covered by round shape oxides with a size of less than 5 μm. However, the oxide scale spalls off at some regions (< 5% surface area) and micro-cracks are also visible on the surface of some precipitates, see in Fig. 5 (c). Based on the EDX analysis, the surface layer is enriched in O, Al, and Ti. The atomic % (at.%) ratio of Ti to Al is around 0.9. Another EDX measurement of the spalled region reveals the increased amount of Ti (nearly two times higher than in the general region), while the Al content is constant. Fig. 5 (d) exhibits the surface morphology of the exposed Ti$_3$AlC$_2$ sample. Here, large quantities of pores or a non-closed oxide layer, like "flower" view, are distributed among the whole surface. The EDX analysis shows enrichment of mainly O, Ti and Al on the surface, with an at.% ratio of Ti to Al is 2.6, see Table 3.
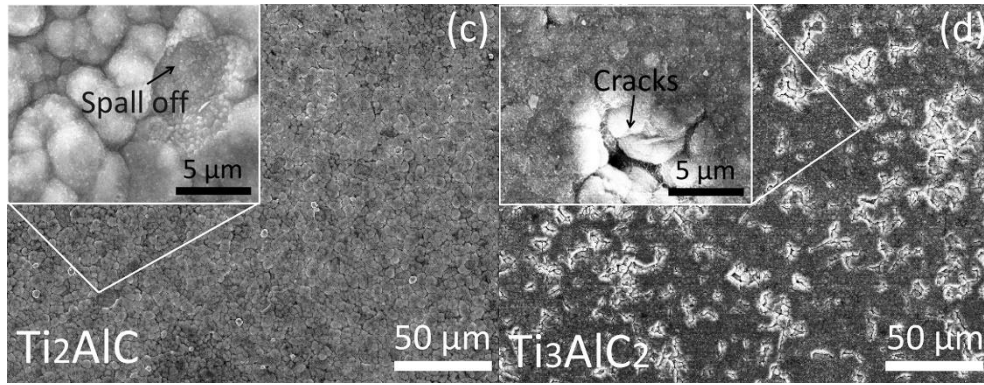
Fig. 5 SEM surface images of MAX-phase coatings (Cr_2AlC, V_2AlC, Ti_2AlC, and Ti_3AlC_2) after the corrosion test.

Table 3
General surface chemical compositions (at.%) of exposed MAX-phase samples, measured by EDX, (applied beam energy: 10 keV).

Sample	O	Al	Cr	Ti	V	Pb	Other
Cr_2AlC	44.8	28.1	5.6	--	--	0.2	Bal.
V_2AlC	29.1	3.1	--	--	13.4	17.8	Bal.
Ti_2AlC	59.6	9.6	--	10.6	--	1.0	Bal.
Ti_3AlC_2	58.1	7.9	--	20.5	--	1.5	Bal.

3.2.3 XPS analysis

Due to the formation of a very thin oxide layer, XRD and SEM/EDX are limited to characterize exclusively the formed oxides. Therefore, XPS has been employed to investigate the chemical compositions of the surface layer more thoroughly.

On the surface of Cr_2AlC after the corrosion test, several elements such as Cr, Al, C, O, Pb, Bi, N, and Mg are detected. Their spectra are shown in Fig 6 (a-d) and Fig. SI-1, respectively. The low intensity of Cr $2p_{3/2}$ peak with binding energy at around 577.3 eV indicates the formation of a low amount of Cr_2O_3. [45] The Al 2p spectrum with Al $2p_{3/2}$ peak at 74.2 eV indicates Al in an oxidized state. The C 1s spectrum in Fig. 4 (c) consists of three peaks at 285.0, 286.3, and 288.4 eV, which is due to the C-C, C-O, and C=O kind of bonds, respectively [26, 46], and they refer to the adventitious carbon species on the surface, and carbides are not detected on the topmost surface. The deconvolution of the O 1s spectra of the Cr_2AlC sample shows a peak at the binding energy of 530.1 eV, which can be assigned to Cr-O [47], as well as Pb-O or Bi-O impurities (shown in Fig. SI-1 (S-a, S-b)). The oxygen peak at 531.3 eV is mainly originated from Al-O bonds and the low intensity peak at 532.7 eV can originate from hydrocarbon impurities (containing C-O bond) on the surface [48-49]. Finally, the identified Mg oxide can be impurities from the molten Pb. Note that the XPS surface measurement is very sensitive even to dilute surface impurities (like remained liquid metals even after washing the samples), it can reveal information at around 10 nm of the top surface.

Figure 6 (E-1) shows the plot of XPS depth profiling in order to characterize the deeper layer of the formed oxide. Until reaching the interface between the oxide and MAX phase coating (after around 60 min of etching), the layer mainly consists of O, Al, and a low amount of Cr (< 3 at.%). The approximate ratio of Al/O is equal to 1.5, confirming the presence of Al_2O_3 mixed with a low amount of chromium oxide. In other words, this depth profile confirms an oxide layer consisting mainly of aluminum oxide with stable stoichiometry on the Cr_2AlC surface. After 60 min etching, a metallic Cr peak (Fig. SI-1 (b)) starts to appear, accompanied by the appearance of carbide C 1s peak (Fig. SI-1 (d)) confirming that the sputter depth profile is approaching the MAX-phase coating [50]. Although the Al 2p oxide peak is still visible, it seems to gradually weaken, as shown in Fig. SI-1 (c).
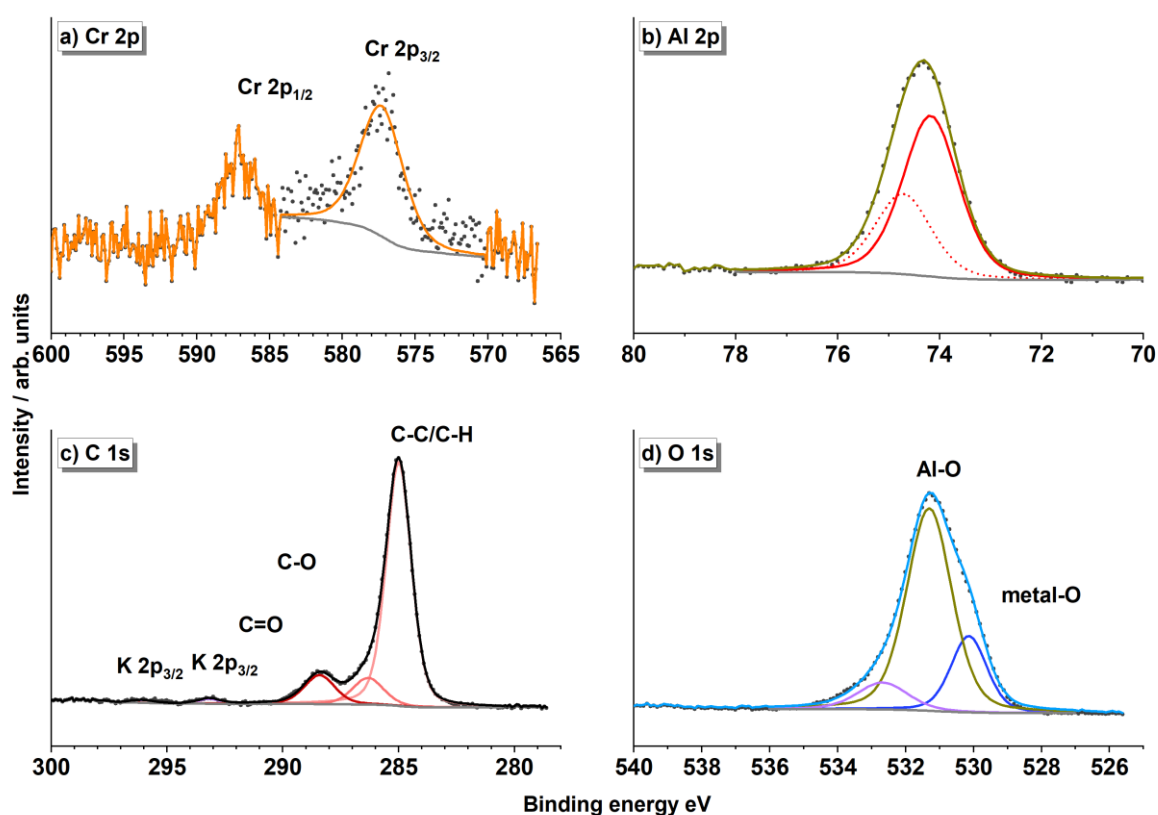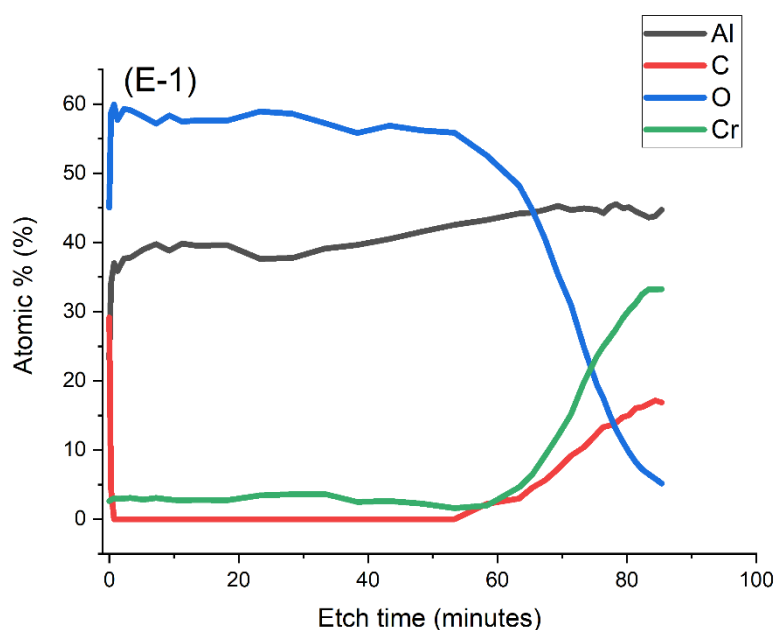
Fig. 6 XPS spectra obtained from Cr$_2$AlC after 3200 h exposure to molten Pb, (a) Cr 2p, (b) Al 2p, (c) C 1s, (d) O 1s; depth profile plot as a function of sputter time (E-1).

Figure 7 shows the surface spectra (a-d) and depth profile (E-2) of the exposed V$_2$AlC. The V 2p$_{3/2}$ peak with the binding energy of 516.9 eV indicates the presence of V$_2$O$_5$ [51-52]. Different from the other MAX phase samples, Al is not detected on the surface of the V$_2$AlC sample. The C 1s spectrum is consisting of adventitious carbon, C-O, and C=O species whereas the related O 1s can be observed at 531.3 eV (C=O) and 532.5 eV (C-O) binding energies [51, 53]. The O 1s peak at 530.0 eV partly originates from V$_2$O$_5$, and partly from remnants of molten lead such as Pb, and Bi oxides as shown in the Fig. SI-2 of the supporting information.

According to the depth profile plot of the liquid metal exposed V$_2$AlC shown in Fig. 7 (E-2), the oxides formed on the surface layer mainly consist of different V oxides, namely VO, VO$_2$, and V$_2$O$_5$ as shown by the shift of the V 2p doublet peaks to lower binding energies in Fig. SI-2 (b). Although it is possible that the V^{5+} is reduced to V^{4+} or V^{2+} as a result of sputter reduction through monoatomic Ar$^+$ ion sputtering during depth profiling. But, this profile gives interesting information that the V$_2$AlC sample doesn't form Al oxide protective layer, and instead there is mainly vanadium oxide present on the surface. Even after a long time etching of the surface, the depth profile still doesn't approach the interface of the oxide layer and MAX phase. In addition, even after 165 min of etching, the Pb and Bi peaks are still present (see Fig. SI-2 (a) of supporting information), which indicates the limited corrosion protectivity of the V-rich oxide layer.
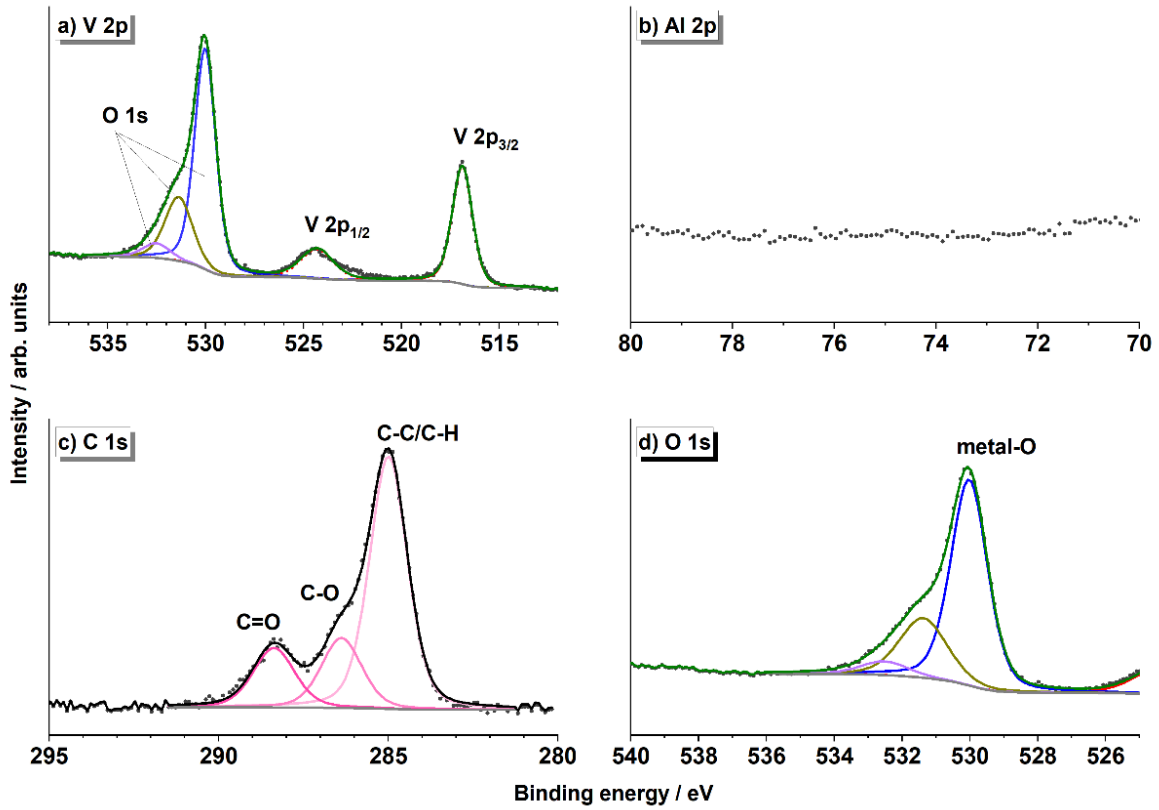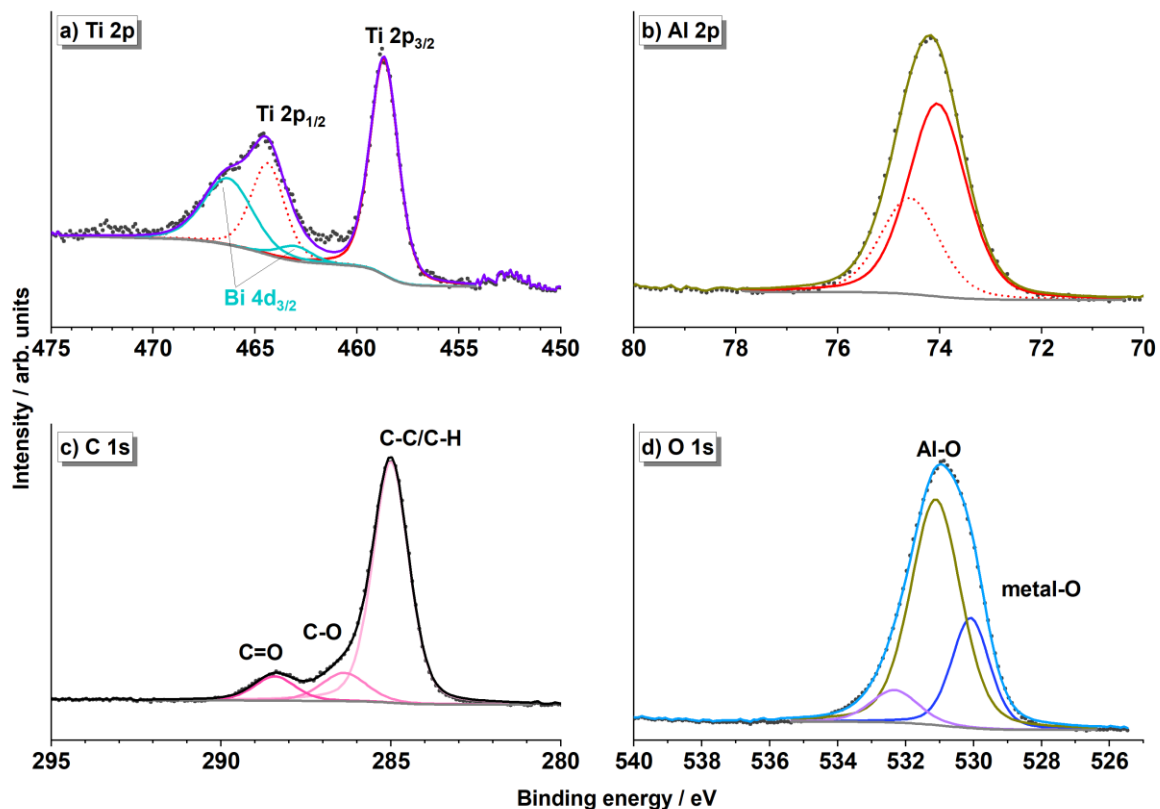
Fig. 7 XPS spectra obtained from V_2AlC after 3200 h exposure to molten Pb, (a) V 2p, (b) Al 2p, (c) C 1s, (d) O 1s; depth profile plot as a function of sputter time (E-2).

The Ti $2p_{3/2}$ peak with the binding energy of 458.7 eV, confirms the presence of titanium oxide on the surface of Ti_2AlC, as shown in Fig. 8 (a) [54-58]. In addition to Ti oxide, Al oxide is also detectable on the surface of Ti_2AlC. The corresponding oxygen peak of Al oxide is also found in the O 1s spectrum with the binding energy of 532.3 eV, see in Fig. 8 (d). The C 1s spectrum observed on

Ti$_2$AlC shows similar peaks to the Cr$_2$AlC sample corresponding to the adventitious carbon species. The identified Bi 4d$_{3/2}$ peak is due to the remained Bi from molten Pb, whereas the spectra of other impurities from molten lead such as Pb 4f, Bi 4f, Sn 3d, and Ag 3d is shown in the supporting information Fig. SI-3.

Figure 8 (E-3) displays the plot of depth profiling of exposed Ti$_2$AlC. Unlike the V$_2$AlC sample, both Al and Ti oxides are present in the oxide layer of Ti$_2$AlC, moreover, the interface between the oxide layer and MAX-phase coating is not so sharp as for the Cr$_2$AlC. After around 35 min of sputter etching, the carbide species in C 1s and Ti 2p spectra are detectable (shown in the supporting information Fig. SI-3 (b, d)). In a closer look at the depth profile, it seems that the near surface region of the Ti$_2$AlC sample is enriched with Al oxide whereas the Ti oxide is more concentrated in the deeper layer near the MAX-phase coating. After around 50 minutes of sputter etching, the profile reaches the MAX-phase, and the Ti oxide completely disappeared whereas the amount of Al oxide and oxygen is continually reducing.
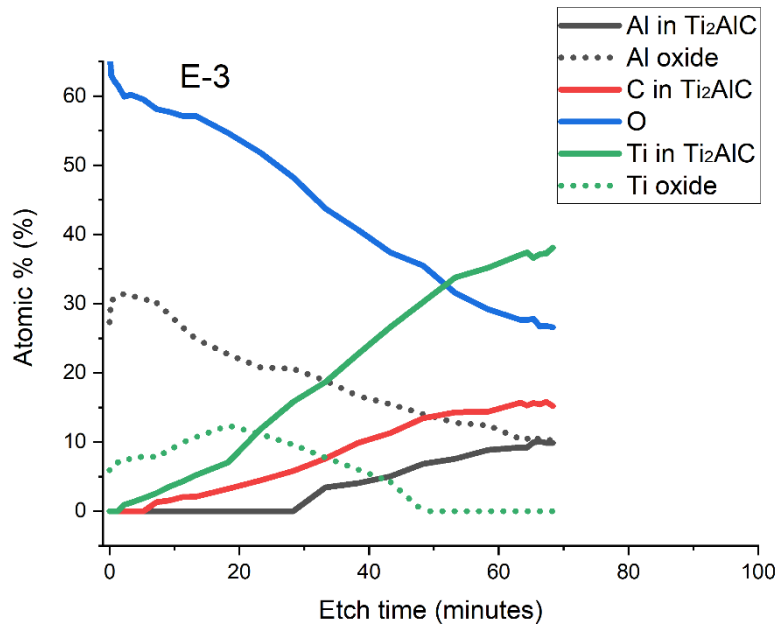
Fig. 8 XPS spectra obtained from Ti_2AlC after 3200 h exposure to molten Pb, (a) Ti 2p, (b) Al 2p, (c) C 1s, (d) O 1s; depth profile plot as a function of sputter time (E-3).

The surface spectra of Ti_3AlC_2 are shown in Fig. 9 (a-d). The Ti $2p_{3/2}$ with a binding energy of 458.3 eV indicates the formation of titanium oxides on the surface. The detected satellite peaks are due to the energy loss of ejected photoelectrons [57-58]. A relatively low intensity Al 2p peak is also detected on the surface. In addition to similar adventitious carbon species, a negligible amount of carbonate (at 289.5 eV) is also found on the surface. The O 1s peak at 529.7 has a majority contribution from Ti oxide and a minor amount of impurity oxides from Pb and Bi. Whereas the peak at 531.5 is an overlap of Al oxide peak and C=O species, finally the peak at 533.4 eV can be related to C-O species [51, 59].

The depth profile (Fig. 9 (E-4)) of the exposed Ti_3AlC_2 doesn't approach the interface of the oxide layer and MAX phase coating even after around 70 minutes of sputter etching. Another interesting observation of this profile is that the presence of Al oxide is not so dominant at the oxide layer, and actually, the oxide layer contains also metallic Ti beside Ti and Al oxides, although metallic Ti might be caused to some extent by the reductive effect of monoatomic Ar^+ ion sputtering (see in Fig. SI-4 (b))
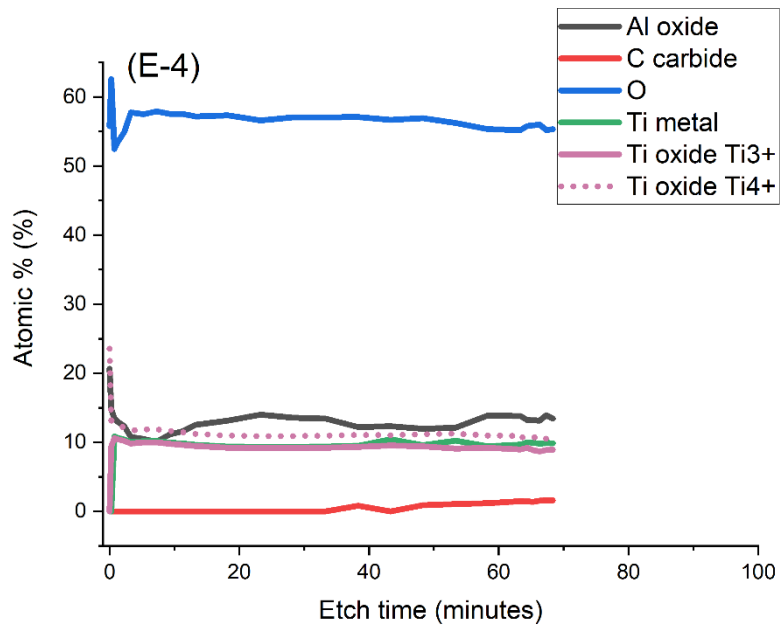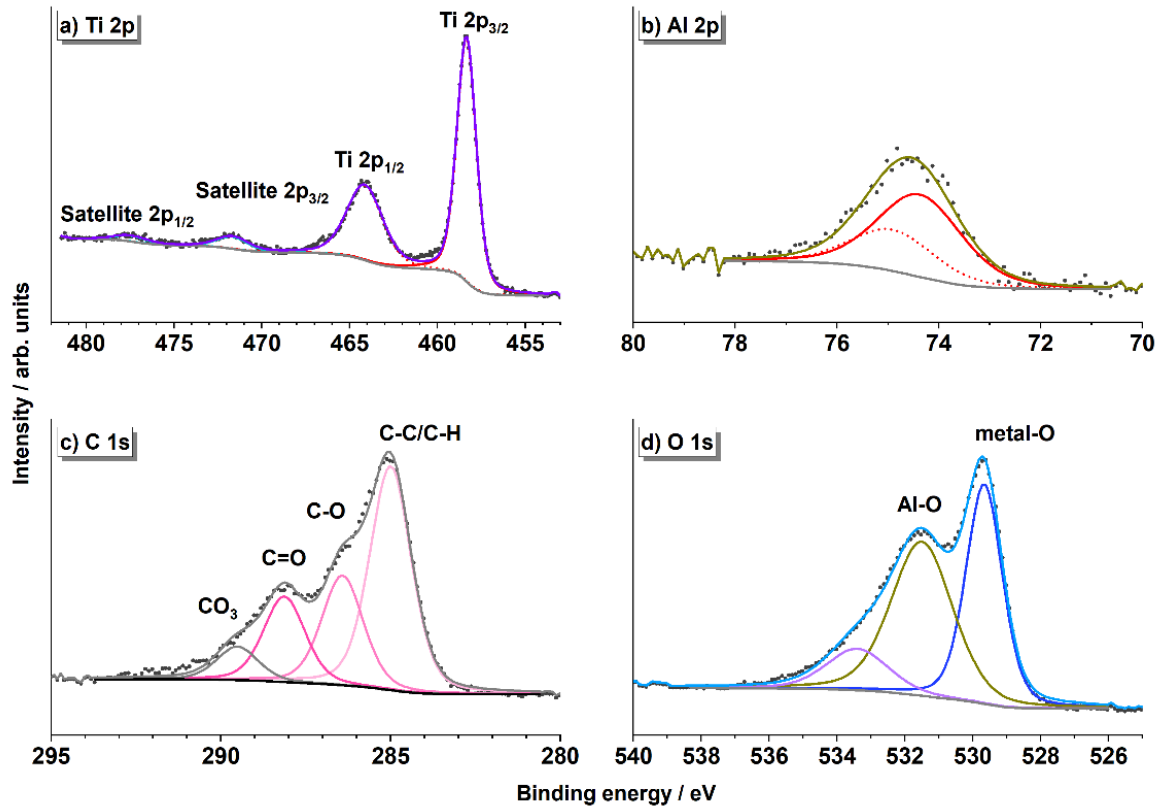
Fig. 9 XPS spectra obtained from Ti_3AlC_2 after 3200 h exposure to molten Pb, (a) Ti 2p, (b) Al 2p, (c) C 1s, (d) O 1s; depth profile plot as a function of sputter time (E-4).

3.2.4 Cross-section analysis

In addition, the cross-sections of exposed samples are characterized to better understand their microstructural evolution and corrosion behavior.

Figure 10 presents the cross-section images of Cr_2AlC. A quite thin layer, shown in dark contrast, is observed above the MAX-phase coating matrix, marked on Fig. 10 (a, b). The thickness measured at different regions varies from 0.2 to 0.3 µm. Both EDX mapping and line scan show coincided signals of O and Al in the oxide layer region. The signal from Cr is weak, which is also confirmed by the XPS measurement, but still visible. Moreover, both SEM surface measurement and XPS analysis have confirmed the partial oxidation of Cr.
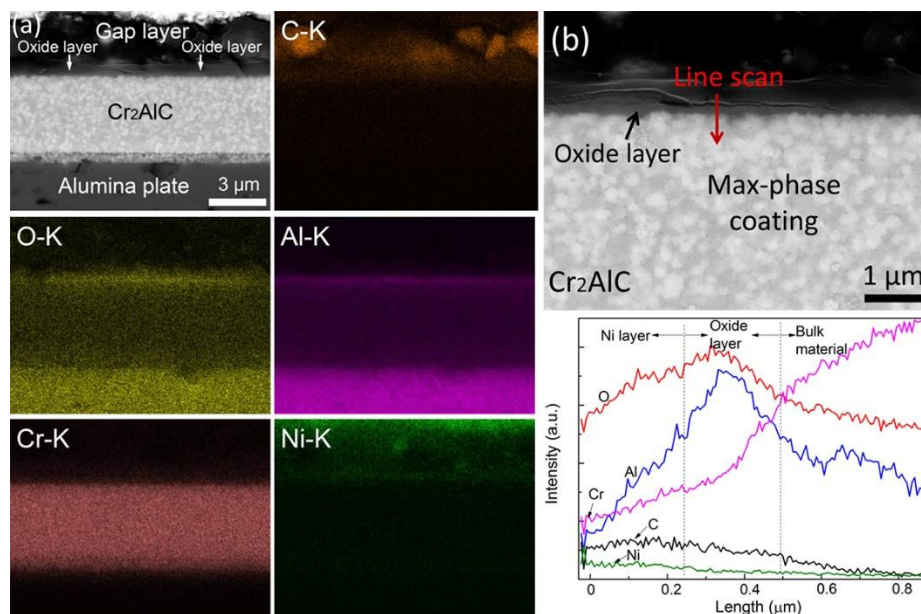

Fig. 10 The cross-sectionnal SEM-EDX images of Cr_2AlC after the corrosion exposure, (a): EDX elemental mapping; (b): EDX line scan acrossing the oxide layer.

The oxide layer cross section of V_2AlC is displayed in Fig. 11. The upper part of the oxide layer (close to the surface) has shown a different roughness. Some parts of the regions are even penetrating into the Ni-layer. The thickness of the oxide layer is around 1.0 to 1.3 µm. Below the oxide layer, there is only a small part of the MAX-phase left, marked on the image (Fig. 11 (b)). It is indicated that the V_2AlC coating is almost entirely consumed by the oxidation during exposure. EDX measurements show the enrichment of O, V, and probably Al (line scan) in the oxide layer region.
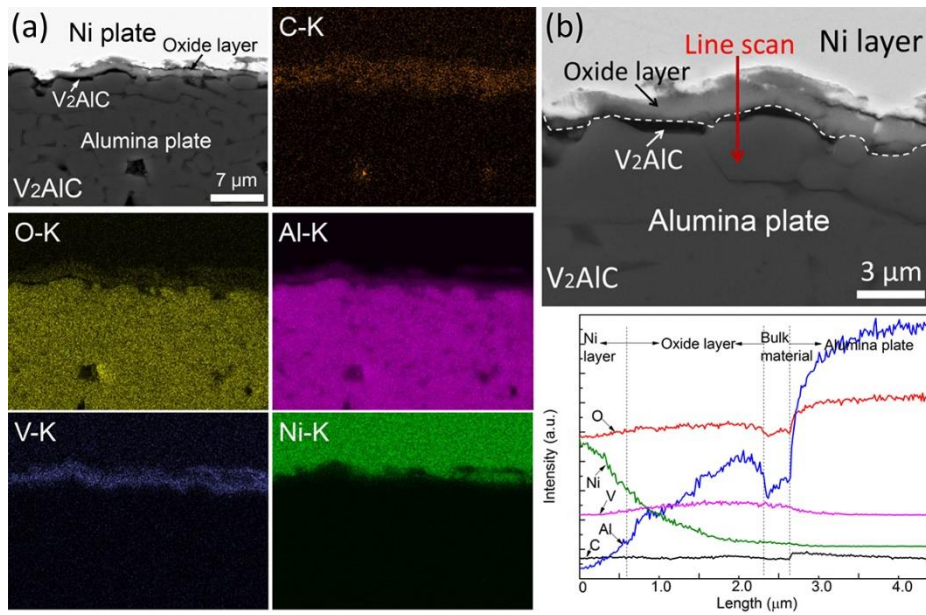
Fig. 11 The cross-sectionnal SEM-EDX images of V$_2$AlC after the corrosion exposure, (a): EDX elemental mapping; (b): EDX line scan acrossing the oxide layer.

Figure 12 displays the cross-section analysis of Ti$_2$AlC. The oxide layer formed on this sample is thicker than that of Cr$_2$AlC. The thickness is in the range of 1.5 to 2.0 μm. EDX analysis indicates the enrichment of O, Al, and Ti, where the signals maxima of Ti and Al coincide. In addition, a thin layer with dark contrast is visible at the interface of the oxide layer and MAX-phase matrix, see the image in Fig. 12 (b). However, no significant difference in chemical compositions is identified between the oxide layer and this dark layer. It might be a transitional layer formed during the corrosion/oxidation [15, 60-61]. Some regions show the oxide scale spallation at the upper part and microcracks, as observed from the surface (Fig. 5). However, these defects only happen at the very surface region (less than 0.5 μm), do not pass through the whole oxide layer.
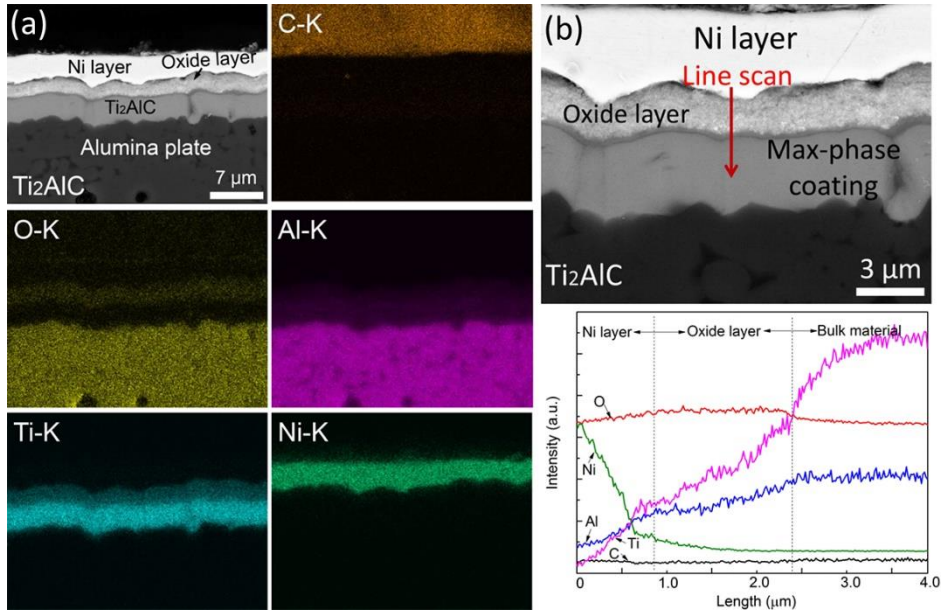
Fig. 12 The cross-sectionnal SEM-EDX images of Ti₂AlC after the corrosion exposure, (a): EDX elemental mapping; (b): EDX line scan acrossing the oxide layer.

Figure 13 shows the SEM-EDX cross-section of the exposed Ti$_3$AlC$_2$. A uniform oxide layer with a thickness comparable to the MAX-phase coating has formed. The surface region of the oxide layer (around 0.3 μm) is bright, which is due to the Pb penetration. The "flower" features (Fig. 5 (d)) are only observed at the very surface region. The total thickness of the oxide layer is around 2.0 to 2.3 μm. According to the EDX analysis, coincided signals of O, Al, and Ti are detected in the oxide layer. The result is also consistent with the XPS measurement, which means the enrichment of Ti- and Al-oxides.
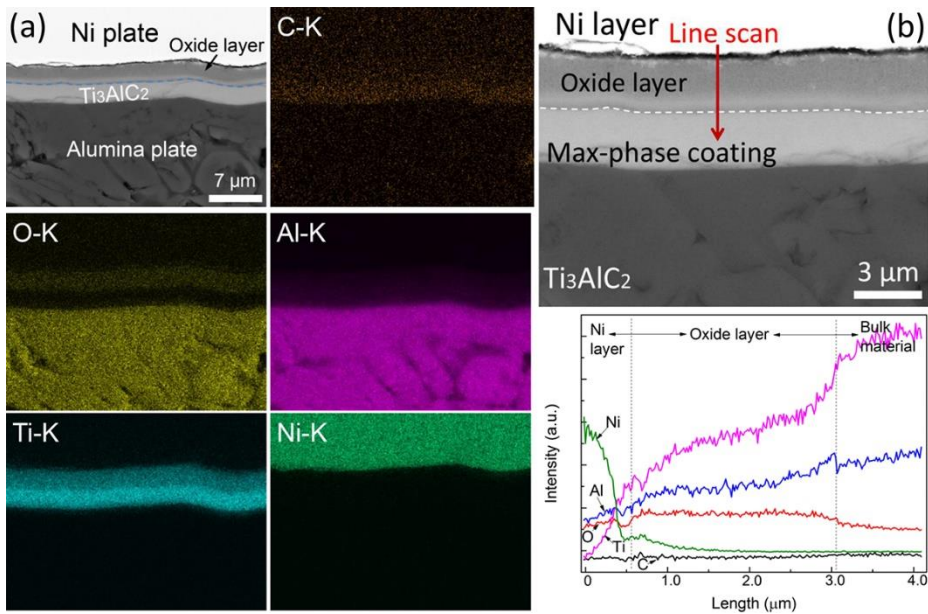

Fig. 13 The cross-sectionnal SEM-EDX images of Ti$_3$AlC$_2$ after the corrosion exposure, (a): EDX elemental mapping; (b): line scan profiles across the oxide layer.

20

3.2.5 TEM characterization of oxide layers

Figure 14 displays the TEM-BF image and the SAED diffraction patterns of the oxide layer formed on Cr_2AlC. The thickness of the oxide layer is approximately 0.3 µm. The BF image shows a relatively homogeneous oxide layer, while the white band is an artefact from sample preparation. The diffraction spots are distributed in a ring shape (but not a ring) which indicates the formation of well-crystallized, nano- and poly-crystalline oxides. The individual diffraction spots can be attributed to the corundum phase alumina, a-Al_2O_3. It should contain some Cr content since Cr_2O_3 can form solid solution with Al_2O_3 [62]. This result is also consistent with the GIXRD and XPS results.
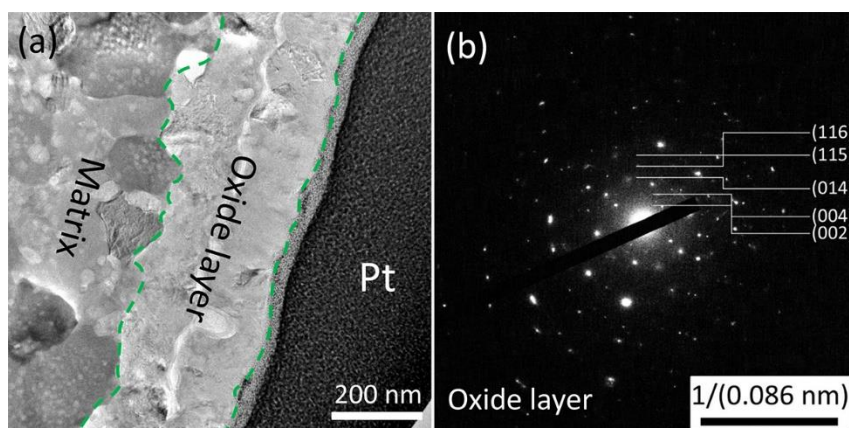

Fig. 14 TEM-BF image of the cross section of Cr_2AlC (a), and corresponding SAED patterns of the oxide layer (b) after the corrosion exposure.

Figure 15 shows the results of TEM-EDS mapping across the oxide layer and the substrate of Cr_2AlC. In general, two zones within the oxide layer can be defined, zone A and zone B, marked on the left cross section image shown in Fig. 15. The thickness of both zones is similar, around half of the whole oxide layer. According to the EDS mapping, the oxidized layer with strong signals of O, Al and C (from sample preparation) is observed. The intensities of O and Al in zone A are lower than that of zone B, and both elements distribute more densely in zone B.
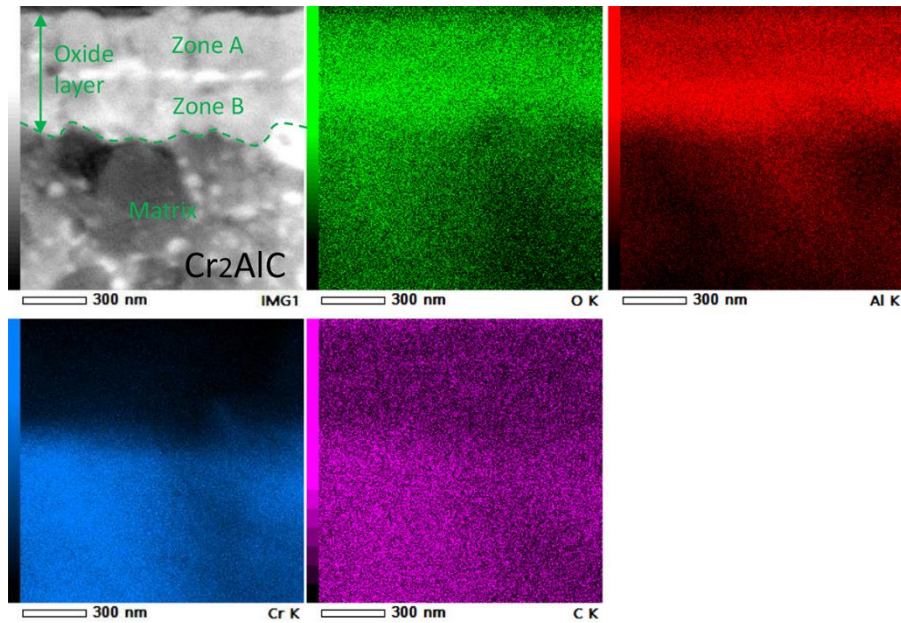
Fig. 15 TEM EDS elemental mapping of the oxide layer formed on Cr_2AlC after the corrosion exposure.

Figure 16 shows results of the TEM analysis of the oxide layer formed on Ti_2AlC. The cross-sectional BF image in Figure 16 (a) clearly shows two layered surface structure. The upper part of the layer, called outer layer, with a rough morphology, has a thickness of around 1.5 μm. The bright spots randomly distributed within the oxide layer are pores induced by the FIB milling process. Below this rough layer, a thin, smooth and dense layer, called inner layer, is identified. The thickness of this layer is around 0.6 μm. The interface between the inner layer and the remaining substrate, called matrix in Figure 16 (a), is relatively sharp, while the interface between the smooth inner and rough outer layer appears more irregular. The SAED diffraction patterns, taken from both the inner layer and outer layer, have been shown in Fig. 16 (b, c), respectively. Both patterns show ring shapes, while the ring circles from the inner layer is more visible than that of the outer layer. This result indicates that the inner layer is less crystallized than the outer layer. According to the previous study by XRD, GIXRD, SEM/EDX and XPS depth profile, the types of oxides formed are TiO_2 and Al_2O_3.
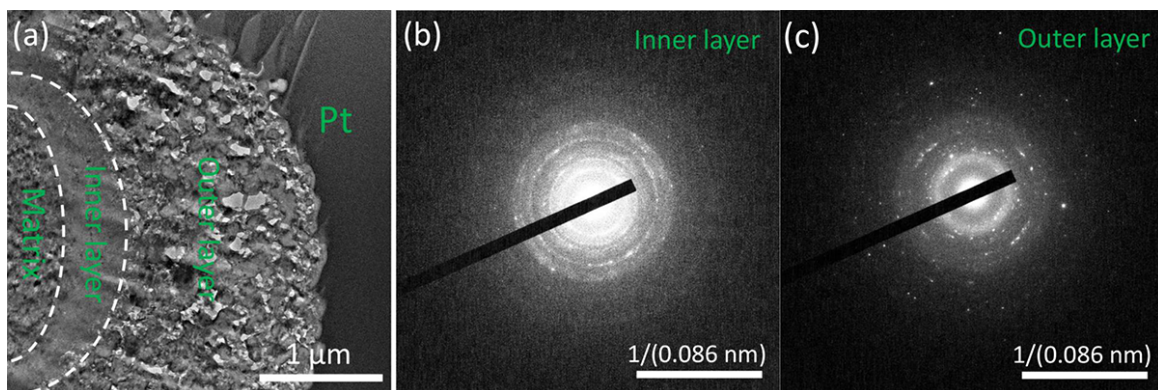

Fig. 16 TEM-BF image of the cross section of Ti_2AlC (a), and corresponding SAED patterns of the oxide layer after the corrosion exposure; (b)inner layer; (c) outer layer

Figure 17 displays results of the TEM-EDS elemental mapping across the oxide layer and the substrate of Ti$_2$AlC. Elements including O, Al and Ti are enriched both in the outer and inner layer. The signal of O is stronger at the inner layer, while the signals of Al and Ti have no clear difference in the outer and inner layer. These results further confirm the formation of mixture of TiO$_2$ and Al$_2$O$_3$ in the oxide layer. The different morphologies of the outer and inner layer might be caused by the chemical gradient, as indicated by the XPS depth profile (Fig. 8).
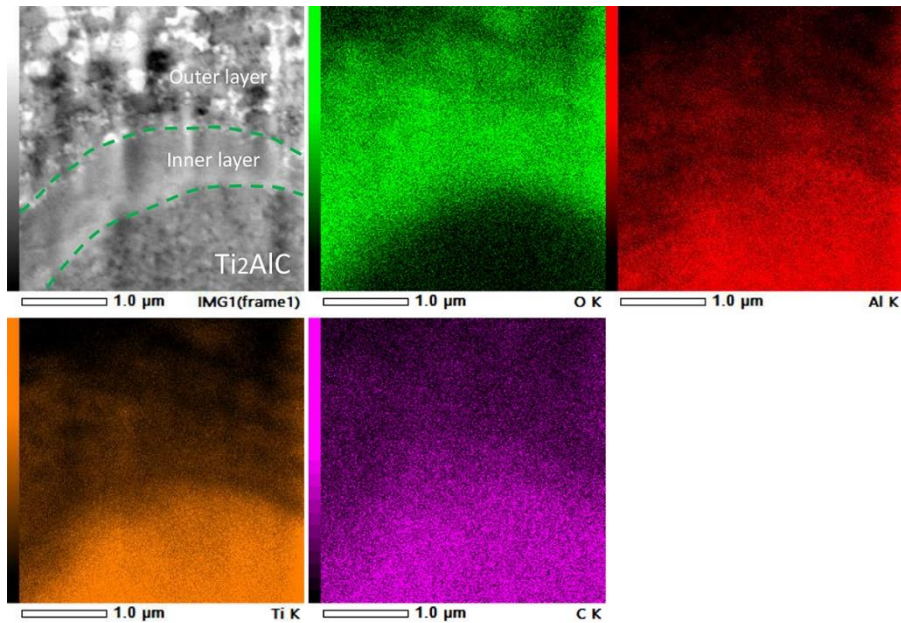

Fig. 17 TEM EDS elemental mapping of the oxide layer formed on Ti$_2$AlC after the corrosion exposure.

4. Discussion

According to the corrosion performance of each MAX-phase coating, their corrosion resistance to heavy liquid metal can be ordered as follows: Cr$_2$AlC > Ti$_2$AlC > Ti$_3$AlC$_2$ > V$_2$AlC. Although the V$_2$AlC coating is nearly consumed during exposure, all of the samples are able to form an oxide layer after 3200 h exposure to molten Pb. The chemical composition and thickness of the oxide layer formed on each sample are summarized in Table 4. Specifically, only the Cr$_2$AlC has formed an alumina dominant layer, while the rest have formed oxides mixture, V-rich or Ti-rich oxides containing alumina. This is determined by their different corrosion mechanisms.

Table 4

General description of the oxide layer formed on each MAX-phase coating.

Sample	Chemical composition	Thickness (µm)
Cr$_2$AlC	Nearly pure Al$_2$O$_3$ (< 3 at.% Cr dissolved)	0.2~0.3 (no spallation)
V$_2$AlC	Mainly V-O mixture (e.g. VO$_2$, V$_4$O$_7$, Pb$_3$(VO$_4$)$_2$)	1.0~1.3 (residual oxide layer, spallation observed)

Ti₂AlC	Al$_2$O$_3$+TiO$_2$ mixture	1.5~2.0 (spallation at some spots)
Ti₃AlC₂	Al$_2$O$_3$+TiO$_2$ mixture	2.0~2.3 (spallation at some spots)

During the oxidation at elevated temperature, alumina with various crystal structures, namely, stable α-Al$_2$O$_3$ (corundum), meta-stable γ-Al$_2$O$_3$, and θ-Al$_2$O$_3$ can form depending mainly on the oxidation temperature and time [63-64]. Generally, the α-Al$_2$O$_3$ is formed at a temperature above 900 °C while meta-stable alumina is formed at lower temperatures [63-64]. However, the metastable Al$_2$O$_3$ is not identified in the current study by XRD and GIXRD. Although the α-Al$_2$O$_3$ signal obtained by the XRD and GIXRD can be influenced by the alumina coating plate, the signals obtained by GIXRD are mainly from a surface layer (0-1000 nm [44]). Considering the information depth of GIXRD and the relatively thick MAX-phase coating (> 3 μm) between the passivating oxide layer and the alumina coating plate (e.g. Fig. 10, Fig. 12 and Fig. 13), the missing signals from the metastable alumina structures indicate the formation of the stale α-Al$_2$O$_3$ only. Therefore, we can conclude that the alumina (corundum) is mainly from the oxide layer, namely Cr$_2$AlC, Ti$_2$AlC and Ti$_3$AlC$_2$. Possible explanations for the corundum-alumina formation include the transition of meta-stable θ-/γ- Al$_2$O$_3$ to stable α-Al$_2$O$_3$ after 3200 h thermal aging, and that corundum Cr$_2$O$_3$ provides nucleation sites for α-Al$_2$O$_3$ (Cr$_2$AlC) [15-16, 56]. In the case of the V$_2$AlC, only a thin MAX-phase coating remains after the exposure (Fig. 11).

As described in the literature [22, 65], the low bonding strength of C-Al leads to the selective oxidation of Al, which is consistent with current experimental results. According to the surface and depth profile of XPS results, the at.% ratio of Al to Cr approaches the formula (Al$_{0.9}$Cr$_{0.1}$)$_2$O$_3$. The concentration of Cr$_2$O$_3$ is low due to the strong bonding of C-Cr. This is also proved by the precipitation of Cr$_7$C$_3$ measured by the XRD after corrosion exposure (Fig. 1 and Table 2). Moreover, the Cr also plays the role of "third element effect" (which describes the reducing critical amount of Al for a continuous alumina scale formation [15, 66]). The oxidation mechanism can be described by equation (1) [67]. Due to the relatively low growth rate of the alumina scale, the oxide layer formed on Cr$_2$AlC is the thinnest among the MAX-phase coatings.

$$Cr_2AlC + O \rightarrow Cr_7C_3 + Al_2O_3 + CO/CO_2 \uparrow \qquad\qquad (1)$$

The V$_2$AlC coating is nearly consumed during the exposure. Instead, multiple V-rich oxides with different valence states have formed. Based on XRD, GIXRD, and XPS results, the V-oxide can be summarized as VO$_2$, V$_4$O$_7$, and Pb$_3$(VO$_4$)$_2$. The V-rich oxide layer is less protective when compared with Al-rich or Ti-rich oxide layer. This is reflected by the oxide scale spallation or the formation of Pb- and V-containing oxide (e.g. Pb$_3$(VO$_4$)$_2$). In addition, the chemical removal of remained Pb by liquid acid solution (hydrogen peroxide, acetic acid and ethanol) might locally influence the
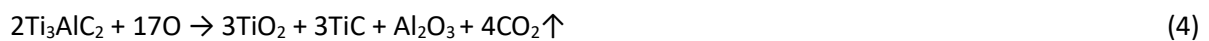
characterization of Pb-rich oxides, which should be considered in the future work. No direct evidence of the Al_2O_3 layer is observed. A low concentration of Al detected by the XPS depth profile (Fig. SI-2 (c)) and EDX line scan (Fig. 10 (right)) might originate from the dissolved Al in V-oxides or the formation of $AlVO_4$ [26, 28]. The oxidation reaction of V_2AlC in oxygen-containing Pb can be described as following reactions (2), (3) [43]:

$$V_2AlC + O \rightarrow V_xO_y + Al_2O_3 + CO/CO_2 \uparrow \tag{2}$$

$$V_2O_5 + PbO \rightarrow Pb_3(VO_4)_2 \tag{3}$$

According to characterization results, the oxide layer formed on Ti_2AlC is a mixture of Al_2O_3 and TiO_2 oxides. Both states of TiO_2, namely rutile and anatase, have been identified. The surface chemical compositions measured by XPS (from surface spectra) reveal that the atomic ratio of Al to Ti is 3.3. The surface composition and depth profile measured by XPS reveals that the Al_2O_3 content is higher than that of TiO_2 within the oxide layer. The literature reported the formation of a separated outer layer of TiO_2 and an inner layer of Al_2O_3 at 900 °C [34], it is different from current results which might be due to low test temperature. In addition, the oxide layer spalls off partially at some spots, which is mainly caused by the mismatch of thermal expansion coefficients [68]. Moreover, the phase transformation of anatase to rutile that happens at 600 °C also results in a crack or even spallation due to the oxide volume shrink [31-32]. However, several investigations have indicated the self-healing ability of the oxide layer grown on Ti_2AlC [68-70].

Since the oxide layer formed on Ti_3AlC_2 has some similarities to Ti_2AlC, they will be discussed together. Both Ti_3AlC_2 and Ti_2AlC have formed the oxide layer based on TiO_2 and Al_2O_3. However, the oxide layer formed on Ti_3AlC_2 is mainly dominated by TiO_2 while Ti_2AlC has formed the mixed layer of TiO_2 and Al_2O_3. Since the Ti-rich oxide layer grows fast [71-72], the oxide layer formed on Ti_3AlC_2 is 1.25 times thicker than that of Ti_2AlC. This might explain why the oxide scale cracking is more severe on Ti_3AlC_2. In addition, the transformation of anatase to rutile, as observed on Ti_2AlC, also contributes to the oxide layer cracking.

According to the literature [31, 54], oxidation of Ti-containing MAX phases is controlled by both inward O diffusion and outward diffusion of Al and Ti. However, the Ti ions are more mobile than the Al ions [71]. The oxidation mechanisms of both MAX-phases can be described by the following reactions (4), (5):

$$2Ti_3AlC_2 + 17O \rightarrow 3TiO_2 + 3TiC + Al_2O_3 + 4CO_2 \uparrow \tag{4}$$

$$2Ti_2AlC + 11O \rightarrow 2TiO_2 + 2TiC + Al_2O_3 + 2CO_2 \uparrow \tag{5}$$

Assuming the same mole % of Ti_3AlC_2 and Ti_2AlC is consumed for the oxidation, the amount of Al_2O_3 produced by Ti_3AlC_2 is the same as that produced by Ti_2AlC, while TiO_2 produced by Ti_3AlC_2 is 1.5 times more. This difference can explain why the oxide layer grown on Ti_3AlC_2 is dominated by TiO_2, while Ti_2AlC has formed mixed oxides of TiO_2 and Al_2O_3.

Besides, all of the MAX-phase coatings have shown relatively high thermal stability after 3200 h exposure at 600 °C. Although carbides like Cr_7C_3, TiC are formed, the decomposition of MAX-phases is mainly caused by an oxidation process. The obtained results are expected to help better understand the protection or degradation mechanism of proposed MAX-phases in HLM environments.

It is necessary to point out that the MAX phase coatings herein are synthesized by thermal annealing of elemental multilayered precursors. The annealing temperature adopted, particularly for Ti_2AlC and Ti_3AlC_2 with 800 °C and 1000 °C annealing temperature, here may exceed the maximum acceptable annealing temperature of the fuel cladding for the HLM-cooled fast reactors. The effect of annealing on the modification of the microstructure and properties of the substrate should be checked. Surface annealing techniques, such as by laser or electron beam, can be adopted to only treat the surface coating layer if these coatings show very promising overall performance for such application. In addition, the corrosion performances obtained here for these four types of MAX phase coatings are only validated for the specific tested conditions with 10^{-6} wt.% oxygen-containing molten Pb at 600 °C. In case of application for Gen-IV Lead-cooled Fast Reactors (LFRs), the test in extreme experiment condition (e.g. temperature > 600 °C or-/and- O concentration $<10^{-6}$ wt.%) should be considered in the future.

5. Conclusions

Four pure Cr_2AlC, V_2AlC, Ti_2AlC, and Ti_3AlC_2 MAX-phase coating samples have been exposed to 10^{-6} wt.% oxygen-containing molten Pb at 600 °C for 3200 h in this study. Based on obtained results, the following conclusions are summarized:

(a) Three MAX-phase coatings (Cr_2AlC, Ti_2AlC, and Ti_3AlC_2) are able to form an oxide layer against the corrosion attack from molten Pb at 600 °C. Although the oxide layer exfoliation is observed on Ti_2AlC and Ti_3AlC_2, no corrosion attack of MAX-phase coating is observed. The V_2AlC coating shows the worst corrosion resistance in molten Pb since it is nearly competely consumed during the exposure.

(b) The Cr_2AlC sample has formed the thinnest oxide scale (< 0.3 μm), while V_2AlC and Ti_2AlC show the oxide scale with a comparable thickness (1.0 to 2.0 μm). Sample Ti_3AlC_2 has formed the

thickest oxide scale (> 2.0 μm).

(c) The type of oxide layer formed on each sample depends on the selective oxidation of alloying elements. Specifically, the Cr_2AlC sample is able to form an Al_2O_3-dominant oxide layer while both Ti_2AlC and Ti_3AlC_2 have formed mixed oxide layers of Al_2O_3 and TiO_2. The V_2AlC has formed a V-rich oxide layer with less protectivity.

(d) Due to the selective oxidation, carbides like Cr_7C_3, TiC have formed below the oxide scale.

Data availability

Acknowledgments

Reference

[1] S. Sen, S. Ganguly, Opportunities, barriers and issues with renewable energy development–A discussion, Renew. Sustain. Energy Rev. 69 (2017) 1170-1181, https://doi.org/10.1016/j.rser.2016.09.137.

[2] S. Chu, A. Majumdar, Opportunities and challenges for a sustainable energy future, Nature 488 (2012) 294-303, https://doi.org/10.1038/nature11475.

[3] D.H. Vo, A.T. Vo, C.M. Ho, H.M. Nguyen, The role of renewable energy, alternative and nuclear energy in mitigating carbon emissions in the CPTPP countries, Renew. Energy 161 (2020) 278-292, https://doi.org/10.1016/j.renene.2020.07.093.

[4] K. Saidi, A. Omri, Reducing CO_2 emissions in OECD countries: Do renewable and nuclear energy matter? Prog. Nucl. Energy 126 (2020) 103425, https://doi.org/10.1016/j.pnucene.2020.103425.

[5] V. Sobolev, Database of thermophysical properties of liquid metal coolants for GEN-IV. Scientific Report SCIENTIFIC REPORT SCK•CEN-BLG-1069, 2011. Mol Belgium, ISSN 1379-2407.

[6] Z. Su'ud, H. Sekimoto, Design and safety aspect of lead and lead-bismuth cooled long-life small safe fast reactors for various fore configurations, J. Nucl. Sci. Technol. 32 (1995) 834-845, https://doi.org/10.1080/18811248.1995.9731785.

[7] H. Kim, D.A. Boysen, J.M. Newhouse, B.L. Spatocco, B. Chung, P.J. Burke, D.J. Bradwell, K. Jiang, A.A. Tomaszowska, K. Wang, W. Wei, Liquid metal batteries: past, present, and future, Chem. Rev. 113 (2013) 2075–2099, https://doi.org/10.1021/cr300205k.

[8] C. Fazio, V.P. Sobolev, A. Aerts, S. Gavrilov, K. Lambrinou, P. Schuurmans, A. Gessi, P. Agostini, A. Ciampichetti, L. Martinelli, S. Gosse, Handbook on Lead-bismuth Eutectic Alloy and Lead Properties, Materials Compatibility, Thermal-hydraulics and technologies-2015 Edition (No. NEA–7268), Organisation for Economic Co-Operation and Development, 2015.

[9] J. Pacio, T. Wetzel, Assessment of liquid metal technology status and research paths for their use as efficient heat transfer fluids in solar central receiver systems, Sol. Energy 93 (2013) 11–22, https://doi.org/10.1016/j.solener.2013.03.025.

[10] D. Frazer, E. Stergar, C. Cionea, P. Hosemann, Liquid metal as heat transport fluid for thermal solar power applications, Energy Procedia 49 (2014) 627–636, https://doi.org/10.1016/j.egypro.2014.03.068.

[11] G. Müller, A. Heinzel, J. Konys, G. Schumacher, A. Weisenburger, F. Zimmermann, V. Engelo, A. Rusanov, V. Markov, Behaviour of steels in flowing liquid PbBi eutectic alloy at 420–600 °C after 4000–7200 h, J. Nucl. Mater. 335 (2004) 163–168, https://doi.org/10.1016/j.jnucmat.2004.07.010.

[12] C. Schroer, O. Wedemeyer, J. Novotny, A. Skrypnik, J. Konys, Selective leaching of nickel and chromium from Type 316 austenitic steel in oxygen-containing lead–bismuth eutectic (LBE), Corros. Sci. 84 (2014) 113–124, https://doi.org/10.1016/j.corsci.2014.03.016.

[13] L. Martinelli, F. Balbaud-Célérier, Modelling of the oxide scale formation on Fe-Cr steel during exposure in liquid lead-bismuth eutectic in the 450–600 ˚C temperature range, Mater. Corros. 62 (2011) 531-542, https://doi.org/10.1002/maco.201005871.

[14] M. Popovic, K. Chen, H. Shen, C. Stan, D. Olmsted, N. Tamura, M. Asta, M. Abad, P. Hosemann, A study of deformation and strain induced in bulk by the oxide layers formation on a Fe-Cr-Al alloy in high-temperature liquid Pb-Bi eutectic, Acta Mater. 151 (2018) 301-309, https://doi.org/10.1016/j.actamat.2018.03.041.

[15] H. Shi, A. Jianu, A. Weisenburger, C. Tang, A. Heinzel, R. Fetzer, F. Lang, R. Stieglitz, G. Müller, Corrosion resistance and microstructural stability of austenitic Fe–Cr–Al–Ni model alloys exposed to oxygen-containing molten lead, J. Nucl. Mater. 524 (2019) 177–190, https://doi.org/10.1016/j.jnucmat.2019.06.043.

[16] H. Shi, R. Fetzer, C.C. Tang, D.V. Szabó, S. Schlabach, A. Heinzel, A. Weisenburger, A. Jianu, G. Müller, The influence of Y and Nb addition on the corrosion resistance of Fe-Cr-Al-Ni model alloys exposed to oxygen-containing molten Pb, Corros. Sci. 179 (2020) 109152. https://doi.org/10.1016/j.corsci.2020.109152.

[17] M.W. Barsoum, The $M_{N+1}AX_N$ phases: A new class of solids: Thermodynamically stable nanolaminates, Prog. Solid State Chem. 28 (2000) 201-281, https://doi.org/10.1016/S0079-6786(00)00006-6.

[18] C. Walter, C. Martinez, T. El-Raghy, J.M. Schneider, Towards large area MAX phase coatings on Steel, Steel Res. Int. 76 (2005) 225-228, https://doi.org/10.1002/srin.200506000.

[19] Z. Wang, G. Ma, L. Liu, L. Wang, P. Ke, Q. Xue, A. Wang, High-performance Cr_2AlC MAX phase coatings: oxidation mechanisms in the 900–1100 °C temperature range, Corros. Sci. 167 (2020) 108492, https://doi.org/10.1016/j.corsci.2020.108492.

[20] C. Torres, R. Quispe, N.Z. Calderón, L. Eggert, M. Hopfeld, C. Rojas, M.K. Camargo, A. Bund, P. Schaaf, R. Grieseler, Development of the phase composition and the properties of Ti2AlC and Ti3AlC2 MAX-phase thin films–A multilayer approach towards high phase purity, Appl. Surf. Sci. 537 (2021) 147864, https://doi.org/10.1016/j.apsusc.2020.147864.

[21] X. Chen, B. Stelzer, M. Hans, R. Iskandar, J. Mayer, J.M. Schneider, Enhancing the high temperature oxidation behavior of Cr_2AlC coatings by reducing grain boundary nanoporosity, Mater. Res. Lett. 9 (2021) 127-133, https://doi.org/10.1080/21663831.2020.1854358.

[22] J. Ward, D. Bowden, E. Prestat, S. Holdsworth, D. Stewart, M.W. Barsoum, M. Preuss, P. Frankel, Corrosion performance of Ti_3SiC_2, Ti_3AlC_2, Ti_2AlC and Cr_2AlC MAX phases in simulated primary water conditions, Corros. Sci. 139 (2018) 444-453, https://doi.org/10.1016/j.corsci.2018.04.034.

[23] B. Tunca, T. Lapauw, C. Callaert, J. Hadermann, R. Delville, N.C. El'ad, M. Dahlqvist, J. Rosén, A.

Marshal, K.G. Pradeep, Compatibility of Zr_2AlC MAX phase-based ceramics with oxygen-poor, static liquid lead–bismuth eutectic, Corros. Sci. 171 (2020) 108704, https://doi.org/10.1016/j.corsci.2020.108704.

[24] D.B. Lee, T.D. Nguyen, S.W. Park, Long-time oxidation of Cr_2AlC between 700 and 1,000 °C in air, Oxid. Met. 77 (2012) 275-287, https://doi.org/10.1007/s11085-012-9285-7.

[25] E. Drouelle, V. Gauthier-Brunet, J. Cormier, P. Villechaise, P. Sallot, F. Naimi, F. Bernard, S. Dubois, Microstructure-oxidation resistance relationship in Ti_3AlC_2 MAX phase, J. Alloys Compd. 826 (2020) 154062, https://doi.org/10.1016/j.jallcom.2020.154062.

[26] C. Azina, S. Mráz, G. Greczynski, M. Hans, D. Primetzhofer, J.M. Schneider, P. Eklund, Oxidation behaviour of V_2AlC MAX phase coatings, J. Eur. Ceram. Soc. 40 (2020) 4436-4444, https://doi.org/10.1016/j.jeurceramsoc.2020.05.080.

[27] Z. Zhang, S.H. Lim, D.M.Y. Lai, S.Y. Tan, X.Q. Koh, J. Chai, S.J. Wang, H. Jin, J.S. Pan, Probing the oxidation behavior of Ti_2AlC MAX phase powders between 200 and 1000 °C, J. Eur. Ceram. Soc. 37 (2017) 43-51, https://doi.org/10.1016/j.jeurceramsoc.2016.08.004.

[28] S. Gupta, M. Barsoum, Synthesis and Oxidation of V_2AlC and $(Ti_{0.5},V_{0.5})_2AlC$ in Air, J. Electrochem. Soc. 151 (2004) D24, https://doi.org/10.1149/1.1639160.

[29] B. Wang, A. Zhou, Q. Hu, L. Wang, Synthesis and oxidation resistance of V_2AlC powders by molten salt method, Int. J. Appl. Ceram. Technol. 14 (2017) 873-879, DOI: 10.1111/ijac.12723.

[30] X. Wang, Y. Zhou, Intermediate-temperature oxidation behavior of Ti_2AlC in air, J. Mater. Res. 17 (2002) 2974-2981, https://doi.org/10.1557/JMR.2002.0431.

[31] W.K. Pang, I.M. Low, B. O'Connor, Z.-M. Sun, K. Prince, Oxidation characteristics of Ti_3AlC_2 over the temperature range 500–900 °C, Mater. Chem. Phys.117 (2009) 384-389, https://doi.org/10.1016/j.matchemphys.2009.06.016.

[32] Z. Lin, M. Li, J. Wang, Y. Zhou, Influence of water vapor on the oxidation behavior of Ti_3AlC_2 and Ti_2AlC, Scr. Mater. 58 (2008) 29-32, https://doi.org/10.1016/j.scriptamat.2007.09.011.

[33] H. Zhang, V. Presser, K.G. Nickel, C. Berthold, Y. Zhou, Hydrothermal oxidation behavior of bulk titanium aluminum carbide, J. Am. Ceram. Soc. 94 (2011) 3460-3466, https://doi.org/10.1111/j.1551-2916.2011.04590.x.

[34] B. Cui, D.D. Jayaseelan, W.E. Lee, TEM study of the early stages of Ti_2AlC oxidation at 900 °C, Scr. Mater. 67 (2012) 830-833, https://doi.org/10.1016/j.scriptamat.2012.07.045.

[35] L. Barnes, N.D. Rago, L. Leibowitz, Corrosion of ternary carbides by molten lead, J. Nucl. Mater. 373 (2008) 424-428, https://doi.org/10.1016/j.jnucmat.2007.04.054.

[36] T. Lapauw, B. Tunca, J. Joris, A. Jianu, R. Fetzer, A. Weisenburger, J. Vleugels, K. Lambrinou, Interaction of $M_{n+1}AX_n$ phases with oxygen-poor, static and fast-flowing liquid lead-bismuth eutectic, J. Nucl. Mater. 520 (2019) 258-272, https://doi.org/10.1016/j.jnucmat.2019.04.010.

[37] A. Heinzel, A. Weisenburger, G. Müller, Long-term corrosion tests of Ti_3SiC_2 and Ti_2AlC in oxygen containing LBE at temperatures up to 700 °C, J. Nucl. Mater. 482 (2016) 114-123, https://doi.org/10.1016/j.jnucmat.2016.10.007.

[38] C. Tang, M. Steinbrück, M. Klimenkov, U. Jäntsch, H.J. Seifert, S. Ulrich, M. Stüber, Textured growth of polycrystalline MAX phase carbide coatings via thermal annealing of M/C/Al multilayers, J. Vac. Sci. Technol A: Vacuum, Surfaces, and Films, 38 (2020) 013401, https://doi.org/10.1116/1.5131544.

[39] C. Tang, M. Große, S. Ulrich, M. Klimenkov, U. Jäntsch, H.J. Seifert, M. Stüber, M. Steinbrück, High-temperature oxidation and hydrothermal corrosion of textured Cr_2AlC-based coatings on zirconium alloy fuel cladding, Surf. Coat. Technol. 419 (2021) 127263, https://doi.org/10.1016/j.surfcoat.2021.127263.

[40] K.L. Parry, A. Shard, R. Short, R. White, J. Whittle, A. Wright, ARXPS characterisation of plasma polymerised surface chemical gradients, Surf. Interface Anal. 38 (2006) 1497-1504, https://doi.org/10.1002/sia.2400.

[41] J. Scofield, Hartree-Slater subshell photoionization cross-sections at 1254 and 1487 eV, J. Electron Spectrosc. Relat. P. 8 (1976) 129-137, https://doi.org/10.1016/0368-2048(76)80015-1.

[42] S. Tanuma, C. Powell, D. Penn, Calculations of electron inelastic mean free paths. IX. Data for 41 elemental solids over the 50 eV to 30 keV range, Surf. Interface Anal. 43 (2011) 689-713, https://doi.org/10.1002/sia.3522.

[43] P.P. Sahoo, E. Gaudin, J. Darriet, T. Guru Row, Synthesis, Characterization, and Crystallographic Study of the PbO−Bi$_2$O$_3$−V$_2$O$_5$ System: Pb$_{3-x}$Bi$_{2x/3}$V$_2$O$_8$ (0.20≤ x≤ 0.50), Inorg. Chem. 49 (2010) 5603-5610, https://doi.org/10.1021/ic100488t.

[44] M. Birkholz, Thin film analysis by X-ray scattering, John Wiley & Sons, 2006.

[45] A. Weisenburger, A. Jianu, S. Doyle, M. Bruns, R. Fetzer, A. Heinzel, M. DelGiacco, W. An, G. Müller, Oxide scales formed on Fe–Cr–Al-based model alloys exposed to oxygen containing molten lead, J. Nucl. Mater. 437 (2013) 282-292, https://doi.org/10.1016/j.jnucmat.2013.02.044.

[46] G. Greczynski, S. Mráz, L. Hultman, J. Schneider, Venting temperature determines surface chemistry of magnetron sputtered TiN films, Appl. Phys. Lett. 108 (2016) 041603, https://doi.org/10.1063/1.4940974.

[47] M. Hassel, I. Hemmerich, H. Kuhlenbeck, H. J. Freund, High resolution XPS study of a thin Cr$_2$O$_3$ (111) film grown on Cr (110), Surf. Sci. Spectra 4 (1996) 246-252, https://doi.org/10.1116/1.1247795.

[48] N. Koslowski, S. Sanctis, R.C. Hoffmann, M. Bruns, J.J. Schneider, Synthesis, dielectric properties and application in a thin film transistor device of amorphous aluminum oxide Al$_x$O$_y$ using a molecular based precursor route, J. Mater. Chem. C 7 (2019) 1048-1056, DOI: 10.1039/C8TC04660C.

[49] D. Dixon, D.J. Babu, A. Bhaskar, H.-M. Bruns, J.J. Schneider, F. Scheiba, H. Ehrenberg, Tuning the performance of vanadium redox flow batteries by modifying the structural defects of the carbon felt electrode, Beilstein J. Nanotechnol. 10 (2019) 1698-1706, https://doi.org/10.3762/bjnano.10.165.

[50] M. Rudolphi, M. Bruns, H. Baumann, U. Geckle, High purity Si–C–N thin films with tailored composition on the tie line SiC–Si$_3$N$_4$, Diam. Relat. Mater. 16 (2007) 1273-1277, https://doi.org/10.1016/j.diamond.2006.12.037.

[51] G. Silversmit, D. Depla, H. Poelman, G.B. Marin, R. De Gryse, Determination of the V2p XPS binding energies for different vanadium oxidation states (V^{5+} to V^{0+}), J ELECTRON SPECTROSC, 135 (2004) 167-175, https://doi.org/10.1016/j.elspec.2004.03.004.

[52] E. Hryha, E. Rutqvist, L. Nyborg, Stoichiometric vanadium oxides studied by XPS, Surf. Interface Anal. 44 (2012) 1022-1025, https://doi.org/10.1002/sia.3844.

[53] S. Ng, P. Fu, W.-L. Yu, H. Chan, K. Tan, Electrically conducting poly [3-(ω-hydroxyalkyl) thiophenes], Synth. Met. 87 (1997) 119-122, https://doi.org/10.1016/S0379-6779(96)04899-0.

[54] Z. Zhang, S.H. Lim, D.M.Y. Lai, S.Y. Tan, X.Q. Koh, J. Chai, S.J. Wang, H. Jin, J.S. Pan, Probing the oxidation behavior of Ti$_2$AlC MAX phase powders between 200 and 1000 °C, J. Eur. Ceram. Soc. 37 (2017) 43-51, https://doi.org/10.1016/j.jeurceramsoc.2016.08.004.

[55] C. Tang, M. Steinbrück, M. Große, T. Bergfeldt, H.J. Seifert, Oxidation behavior of Ti$_2$AlC in the temperature range of 1400 °C–1600 °C in steam, J. Nucl. Mater. 490 (2017) 130-142, https://doi.org/10.1016/j.jnucmat.2017.03.016.

[56] J. Chastain, R.C. King Jr, Handbook of X-ray photoelectron spectroscopy, Perkin-Elmer, USA, 1992.

[57] G. Vernon, G. Stucky, T.A. Carlson, Comprehensive study of satellite structure in the photoelectron spectra of transition metal compounds, Inorg. Chem. 15 (1976) 278-284.

[58] A.A. Pustovalova, V.F. Pichugin, N.M. Ivanova, M. Bruns, Structural features of N-containing titanium dioxide thin films deposited by magnetron sputtering, Thin solid films, 627 (2017) 9-16, https://doi.org/10.1016/j.tsf.2017.02.056.

[59] F. Fedorov, M. Vasilkov, A. Lashkov, A. Varezhnikov, D. Fuchs, C. Kübel, M. Bruns, M. Sommer, V. Sysoev, Toward new gas-analytical multisensor chips based on titanium oxide nanotube array, Sci. Rep. 7 (2017) 1-9, https://doi.org/10.1038/s41598-017-10495-8.

[60] H. Shi, A. Jianu, R. Fetzer, D.V. Szabó, S. Schlabach, A. Weisenburger, C. Tang, A. Heinzel, F. Lang, G. Müller, Compatibility and microstructure evolution of Al-Cr-Fe-Ni high entropy model alloys

exposed to oxygen-containing molten lead, Corros. Sci. (2021) 109593, https://doi.org/10.1016/j.corsci.2021.109593.

[61] H. Shi, R. Fetzer, A. Jianu, A. Weisenburger, A. Heinzel, F. Lang, G. Müller, Influence of alloying elements (Cu, Ti, Nb) on the microstructure and corrosion behaviour of AlCrFeNi-based high entropy alloys exposed to oxygen-containing molten Pb, Corros. Sci. (2021) 109659, https://doi.org/10.1016/j.corsci.2021.109659.

[62] P. Zhao, H. Zhao, J. Yu, H. Zhang, H. Gao, Q. Chen, Crystal structure and properties of Al2O3-Cr2O3 solid solutions with different Cr2O3 contents, Ceram. Int. 44 (2018) 1356-1361, https://doi.org/10.1016/j.ceramint.2017.08.195.

[63] R. Prescott, M. Graham, The oxidation of iron-aluminum alloys, Oxid. Met. 38 (1992) 73-87, https://doi.org/10.1007/BF00665045.

[64] R. Cueff, H. Buscail, E. Caudron, C. Issartel, F. Riffard, Oxidation of alumina formers at 1173 K: effect of yttrium ion implantation and yttrium alloying addition, Corros. Sci. 45 (2003) 1815-1831, https://doi.org/10.1016/S0010-938X(02)00254-8.

[65] O. Berger, R. Boucher, M. Ruhnow, Part I. Mechanism of oxidation of Cr_2AlC films in temperature range 700–1200 °C, Surf. Eng. 31 (2015) 373-385, https://doi.org/10.1179/1743294414Y.0000000417.

[66] C. Wagner, Passivity and inhibition during the oxidation of metals at elevated temperatures, Corros. Sci. 5 (1965) 751-764, https://doi.org/10.1016/S0010-938X(65)80003-8.

[67] Z. Lin, M. Li, J. Wang, Y. Zhou, High-temperature oxidation and hot corrosion of Cr_2AlC, Acta Mater. 55 (2007) 6182-6191, https://doi.org/10.1016/j.actamat.2007.07.024.

[68] S. Li, G. Song, K. Kwakernaak, S. van der Zwaag, W.G. Sloof, Multiple crack healing of a Ti_2AlC ceramic, J. Eur. Ceram. Soc. 32 (2012) 1813-1820, https://doi.org/10.1016/j.jeurceramsoc.2012.01.017.

[69] Y. Du, J.X. Liu, Y. Gu, X.G. Wang, F. Xu, G.J. Zhang, Anisotropic corrosion of Ti_2AlC and Ti_3AlC_2 in supercritical water at 500 °C, Ceram Int. 43 (2017) 7166-7171, https://doi.org/10.1016/j.ceramint.2017.02.153.

[70] G. Song, Y. Pei, W. Sloof, S. Li, J.T.M. De Hosson, S. Van der Zwaag, Oxidation-induced crack healing in Ti_3AlC_2 ceramics, Scr. Mater. 58 (2008) 13-16, https://doi.org/10.1016/j.scriptamat.2007.09.006.

[71] A. Donchev, M. Schütze, Minimization of the Oxygen Embrittlement of Ti-Alloys, Theodor-Heuss-Allee, 25 (2021) 60486, retrieved on 08.08.2021.

[72] H. Shi, C. Tang, A. Jianu, R. Fetzer, A. Weisenburger, M. Steinbrueck, M. Grosse, R. Stieglitz, G. Müller, Oxidation behavior and microstructure evolution of alumina-forming austenitic & high entropy alloys in steam environment at 1200 °C, Corros. Sci. 170 (2020) 108654, https://doi.org/10.1016/j.corsci.2020.108654